Title: TOLLIP resolves lipid-induced EIF2 signaling in alveolar macrophages for durable *Mycobacterium tuberculosis* protection.

One Sentence Summary: In *M. tuberculosis*-infected alveolar macrophages, TOLLIP deficiency induces lipid accumulation, which activates EIF2 signaling and prevents durable *M. tuberculosis* protection *in vivo*.

Authors: Sambasivan Venkatasubramanian[1], Courtney Plumlee[2], Kim Dill-McFarland[1], Gemma L. Pearson[3], Sara B. Cohen[2], Anne Lietzke[3], Amanda Pacheco[3], Sarah A. Hinderstein[1], Robyn Emery[1], Scott A. Soleimanpour[3,4], Matthew Altman[1], Kevin B. Urdahl[2,5], Javeed A. Shah[1,6*].

Affiliations:

[1] Department of Medicine, University of Washington, Seattle, WA.

[2] Seattle Children's Research Institute, Seattle, WA.

[3] Department of Internal Medicine, University of Michigan, Ann Arbor, MI.

[4] VA Ann Arbor Healthcare System, Ann Arbor, MI.

[5] Departments of Pediatrics and Immunology, University of Washington, Seattle, WA.

[6] VA Puget Sound Healthcare System, Seattle, WA.

20 *Corresponding author: Javeed A. Shah; jashah@uw.edu

21

Abstract:

Relative deficiency of TOLLIP expression in monocytes is associated with increased tuberculosis (TB) susceptibility in genetic studies, despite antagonizing host innate immune pathways that control *Mycobacterium tuberculosis* (Mtb) infection. In this study, we investigated the mechanisms by which TOLLIP influences Mtb immunity. *Tollip*$^{-/-}$ mice developed worsened disease, consistent with prior genetic observations, and developed large numbers of foam cells. Selective TOLLIP deletion in alveolar macrophages (AM) was sufficient to induce lipid accumulation and increased Mtb persistence 28 days after infection, despite increased antimicrobial responses. We analyzed sorted, Mtb-infected *Tollip*$^{-/-}$ AM from mixed bone marrow chimeric mice to measure global gene expression 28 days post-infection. We found transcriptional profiles consistent with increased EIF2 signaling. Selective lipid administration to *Tollip*$^{-/-}$ macrophages induced lipid accumulation, and Mtb infection of lipid laden, *Tollip*$^{-/-}$ macrophages induced cellular stress and impaired Mtb control. EIF2 activation induced increased Mtb replication within macrophages, irrespective of TOLLIP expression, and EIF2 kinases were enriched in human caseous granulomas. Our findings define a critical checkpoint for TOLLIP to prevent lipid-induced EIF2 activation and demonstrate an important mechanism for EIF2 signaling to permit Mtb replication within macrophages.

Keywords: TOLLIP, tuberculosis, macrophages, foam cells, innate immunity, integrated stress response, cellular homeostasis, lipid metabolism, autophagy, ER stress, EIF2A

42 **Main Text:**

43 **Introduction**

44 Toll-Interacting Protein (TOLLIP) is a selective autophagy receptor and endosomal
45 sorting protein that was initially identified as a TLR and IL-1R binding protein, (*1*) and
46 chaperones membrane bound receptors and protein aggregates to the autophagosome via
47 endoplasmic reticulum (ER) transport and autophagy (*2, 3*)(*4, 5*). A functionally active single
48 nucleotide polymorphism upstream of the TOLLIP transcriptional start site diminishes TOLLIP
49 gene expression in monocytes and is associated with increased risk for pulmonary and
50 meningeal TB, increased innate immune responses after Mtb infection, and diminished BCG-
51 specific T cell responses in South African infants (*6, 7*). We sought to define the mechanism by
52 which TOLLIP influences Mtb susceptibility, especially during chronic phases of infection.
53 Therefore, we evaluated TOLLIP' mechanism of effect on pulmonary innate immune responses
54 to Mtb infection and TB severity over time, in small animal models. In these papers, identified a
55 critical checkpoint of lipid homeostasis required for durable control in chronically Mtb-infected
56 macrophages.

57 The impact of autophagy machinery on Mtb pathogenesis is incompletely understood.
58 After IFNγ activation, autophagy contributes to host defense within murine macrophages by
59 trafficking Mtb to autophagolysosomes for destruction, but this only represents a partial
60 contribution to Mtb clearance (*8, 9*). Autophagy also dampens innate immune responses,
61 including inflammasome and TLR activity (*10*), and the autophagy regulator Atg5 controls
62 neutrophil-induced tissue destruction and immunopathology after Mtb infection (*11, 12*).

63 Autophagy is also induced to clear misfolded proteins and excess lipid as part of the integrated
64 stress response (ISR), which promotes cell survival and is an important mechanism for
65 maintaining cellular function over time, but its role in Mtb pathogenesis is not well understood
66 (*13*). TOLLIP, an autophagy receptor, is associated with TB susceptibility, so understanding its
67 role in macrophage function may provide insight into how autophagy machinery can influence
68 Mtb pathogenesis.

69 The influence of integrated stress response (ISR) on Mtb pathogenesis is not completely
70 understood. The ISR is induced by excess misfolded protein, lipid, or heat shock, which activate
71 one of four kinases (HRI, GCN2, PERK, and PKR) to phosphorylate EIF2S1 (*14*). EIF2S1
72 phosphorylation induces dramatic changes in cell translation and function, which may lead to
73 adaptation and cellular survival by inducing autophagy or cell death, if stresses are prolonged
74 or severe (*14, 15*). Multiple lines of evidence suggest that the ISR may prevent durable Mtb
75 control. Granulomas are hypoxic, associated with increased lipid content, and are
76 inflammatory, and each of these phenotypes induces the ISR *(16-18)*. The ISR diminishes protein
77 translation and impairs glycolysis, and these phenotypes are associated with decreased
78 macrophage control of Mtb (*19, 20*). Oxidative stress, another inducer of the ISR, in
79 macrophages induces inflammatory overreaction to bacterial products and TNF, which can
80 worsen outcomes from TB infection (*21-24*). Mtb infection of macrophages induces ER stress,
81 but whether this is beneficial by inducing apoptosis or harmful by preventing adequate Mtb
82 control is not certain (*25-27*). In this study, we found that TOLLIP-deficient mice develop
83 selective lipid accumulation in their alveolar macrophages (AM) during Mtb infection,
84 prompting us to test the effects of selective intracellular lipid accumulation on Mtb

85 pathogenesis *in vitro* and *in vivo*. In this absence of clearance, excess lipid induces the ISR and
86 permits Mtb replication, which ultimately leads to Mtb progression.

87 **Results**

88 *Tollip$^{-/-}$ macrophages develop proinflammatory cytokine bias*

89 In preliminary experiments, we identified a functional single nucleotide polymorphism in the
90 TOLLIP promoter region that was associated with decreased TOLLIP mRNA expression in
91 peripheral blood monocytes and hyperinflammatory cytokine responses after TLR stimulation
92 and Mtb infection (*6, 7, 28*). This variant was also associated with increased risk for pulmonary
93 and meningeal TB in genetic studies (*28*). To link these human genetic observations with our
94 small animal model, we evaluated the functional capacity of *Tollip$^{-/-}$* macrophages to produce
95 pro- and anti-inflammatory cytokines after TLR stimulation and Mtb infection. We isolated
96 peritoneal macrophages (PEM), plated them *ex vivo* and stimulated them with LPS (TLR4 ligand;
97 10ng/ml), PAM3 (TLR2/1 ligand; 250ng/ml), or Mtb whole cell lysate (1µg/ml). *Tollip$^{-/-}$* PEM
98 secreted more TNF than control after all stimulation conditions (**Figure S1A**, LPS $p = 0.01$, PAM3
99 $p = 0.002$, Mtb lysate $p = 0.01$, $n = 9$). Conversely, *Tollip$^{-/-}$* PEM induced less IL-10 than controls
100 (**Figure S1B**, LPS $p = 0.01$, PAM3 $p = 0.02$, Mtb lysate $p = 0.03$, $n = 9$). We infected PEM with live
101 Mtb H37Rv strain (MOI 2.5) overnight and measured TNF, IL-1β and IL-10. After infection, *Tollip^{-}*
102 *$^{/-}$* PEM secreted more TNF and IL-1β, while inducing less IL-10 than controls (MOI 2.5) (**Figure**
103 **S1C-E**; $p=0.03$, $p=0.03$, and $p=0.02$ respectively), which is consistent with prior human
104 observations (*7, 28*). Thus, murine TOLLIP recapitulated the functional phenotypes of human
105 TOLLIP after Mtb infection in macrophages.
106

107 *TOLLIP is required to control Mtb infection*

108 A functionally active variant in the TOLLIP promoter was associated with increased TB
109 susceptibility (*6, 7, 28*). This SNP was also associated with 1) decreased TOLLIP mRNA expression
110 in monocytes, 2) increased innate immune responses to Mtb infection, but 3) diminished BCG-
111 specific CD4+ T cell responses, suggesting multiple possible mechanisms by which it may
112 mediate TB progression (*7*). Therefore, we evaluated how TOLLIP influenced TB outcomes in
113 the knockout mouse model to elucidate the mechanistic underpinnings of TOLLIP in the
114 immune response to Mtb *in vivo*. We infected *Tollip*$^{-/-}$ mice and littermate controls expressing
115 *Tollip* (WT) with 100 cfu of Mtb H37Rv strain via aerosol and monitored weight, bacterial colony
116 forming units (CFU), and survival over time (**Figure 1A**). Lung CFU were diminished two weeks
117 after infection in *Tollip*$^{-/-}$ mice ($p < 0.009$, $n = 5$; **Figure 1B**). Four weeks post-infection, Mtb
118 bacterial burden in the lung was diminished in *Tollip*$^{-/-}$ mice compared with controls (**Figure**
119 **1C**, n =30 / mouse type; $p < 0.020$, two-sided t-test). Eight weeks post-infection, this phenotype
120 reversed and *Tollip*$^{-/-}$ mice developed increased bacterial burden ($p=0.0011$, two-sided t-test)
121 and beyond. By 180 days, lung bacterial burdens were increased ten-fold in *Tollip*$^{-/-}$ mice
122 compared to controls ($p = 0.03$, t-test; overall difference in groups, $p = 0.004$, mixed effects
123 model comparing, genotype, time, and TOLLIP expression). Similarly, we found
124 extrapulmonary dissemination of Mtb was delayed in *Tollip*$^{-/-}$ mice, as we were unable to culture
125 Mtb from of 3/5 spleens (**Figure 1D**, $p = 0.06$, two-sided t-test). Four weeks after infection,
126 bacterial load was decreased in the spleens of *Tollip*$^{-/-}$ mice, but we observed increased bacterial
127 burden in the spleen after eight weeks and onward (**Figure 1E**, $p = 0.0092$, 2-way ANOVA
128 comparing time and genotype). *Tollip*$^{-/-}$ mice met criteria for euthanasia a median of 228 days
129 after infection (**Figure 1F**; $p < 0.0001$, $n = 10$ / group, Mantel-Cox test), whereas WT mice did

130 not lose weight and survived over 250 days after infection. *Tollip*$^{-/-}$ mice lost weight beginning
131 approximately 180 days post-infection as well (**Figure 1G**, $p < 0.0001$, 2-way ANOVA
132 accounting for genotype and time). Histopathologic analysis of lung sections also revealed
133 differences between early and late immune responses in *Tollip*$^{-/-}$ mice. Although *Tollip*$^{-/-}$ and WT
134 mice developed qualitatively similar inflammatory lesions four weeks post-infection, by eight
135 weeks post-infection, *Tollip*$^{-/-}$ mice displayed increased numbers of cellular structures with a
136 foamy appearance within infiltrates, consistent with lipid-laden "foamy" macrophages (**Figure**
137 **1H**). Taken together, *Tollip*$^{-/-}$ mice exhibit early resistance to Mtb infection during the first 2-4
138 weeks, which might be predicted by the enhanced inflammatory response of *Tollip*$^{-/-}$
139 macrophages. Paradoxically, during chronic stages of Mtb infection their susceptibility is
140 reversed and *Tollip*$^{-/-}$ mice exhibit higher bacterial burdens than WT controls.

141 Because TOLLIP is ubiquitously expressed (*29*), we generated reciprocal bone-marrow
142 chimeras to assess whether TOLLIP's expression in hematopoietic or non-hematopoietic cells
143 is required for immunity against Mtb. Lung bacterial burdens were assessed in mice infected
144 with Mtb eight weeks prior (**Figure 1G**). Consistent with our results in non-chimeric mice, *Tollip*$^{-}$
145 $^{/-}$ bone marrow -> *Tollip*$^{-/-}$ mice exhibited higher lung bacterial burdens that WT -> WT controls.
146 Importantly, *Tollip*$^{-/-}$ -> WT chimeras had elevated bacterial burdens like *Tollip*$^{-/-}$ -> *Tollip*$^{-/-}$
147 controls, whereas bacterial burdens in WT -> *Tollip*$^{-/-}$ were not significantly different than WT -
148 > WT controls. These data suggest a specific role for TOLLIP in radiosensitive hematopoietic
149 cells during Mtb infection.

150

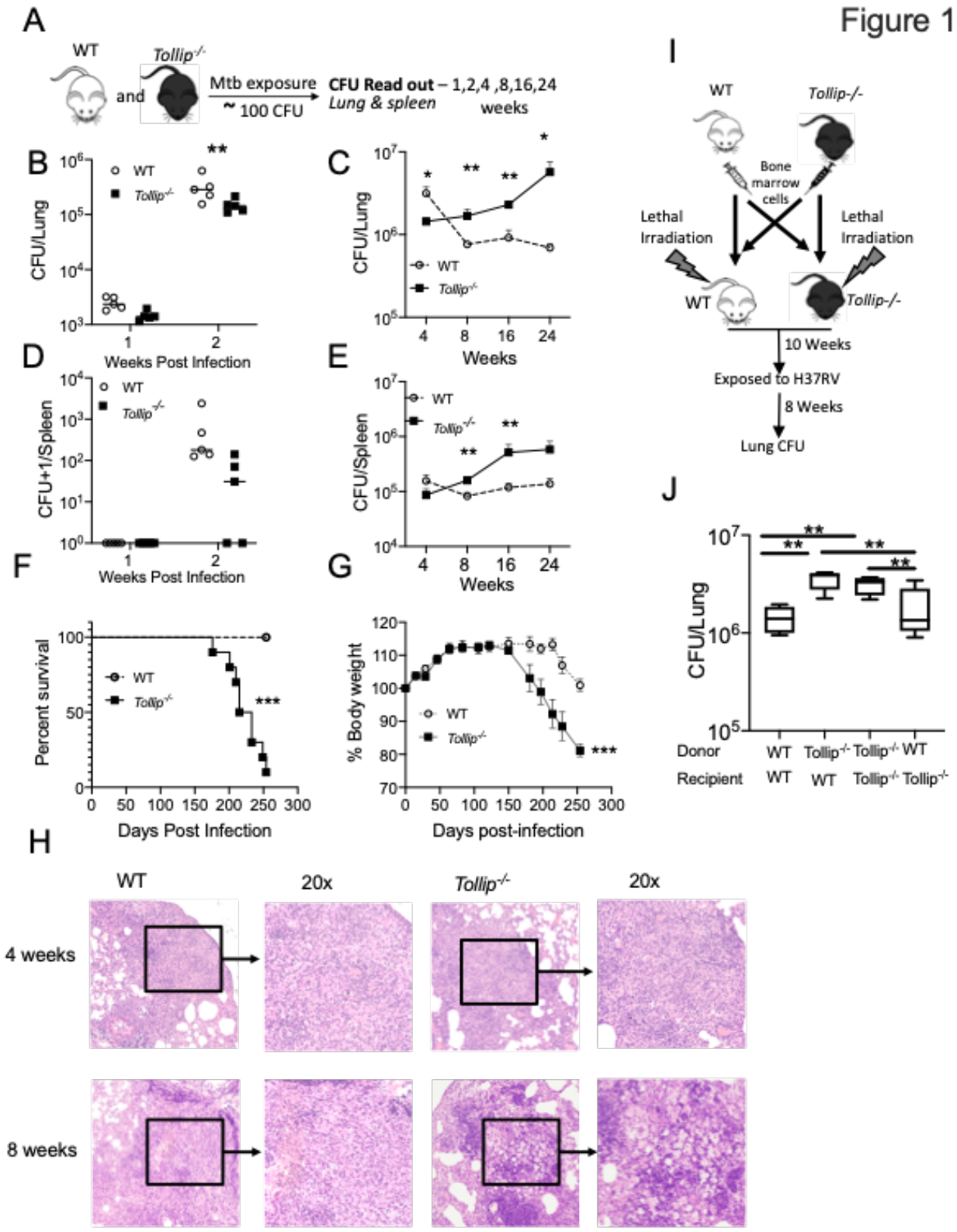
Figure 1
A
WT
Tollip-/-
and
Mtb exposure
~ 100 CFU
CFU Read out – 1,2,4 ,8,16,24 weeks
Lung & spleen
B
CFU/Lung
Weeks Post Infection
C
CFU/Lung
Weeks
D
CFU+1/Spleen
Weeks Post Infection
E
CFU/Spleen
Weeks
F
Percent survival
Days Post Infection
G
% Body weight
Days post-infection
H
WT
20x
Tollip-/-
20x
4 weeks
8 weeks
I
WT
Tollip-/-
Bone marrow cells
Lethal Irradiation
Lethal Irradiation
WT
Tollip-/-
10 Weeks
Exposed to H37RV
8 Weeks
Lung CFU
J
CFU/Lung
Donor
Recipient
WT WT
Tollip-/- WT
Tollip-/- Tollip-/-
WT Tollip-/-

151

152 **Figure 1. TOLLIP is required for Mtb control in mice and its absence induces foam cell**
153 **formation.** Mice were infected with Mtb H37Rv (50-100 cfu) via aerosol and monitored over
154 time. **A)** Experimental timeline. **B-C)** Lung bacterial burden in WT (*clear circle*) and *Tollip*$^{-/-}$ (*black*
155 *square*) mice **B)** 1-2 weeks and **C**) 4 weeks and later after infection. Spleen bacterial burden **D**)
156 1-2 weeks and **E)** 4 weeks and later after infection. * $p < 0.05$; ** $p < 0.01$, ***$p < 0.001$, two-
157 sided t-test at each time point; n = 5 mice/group. Overall associations were determined using
158 a two-sided ANOVA accounting for time and genotype. **F)** Survival curve analysis of WT (*clear*
159 *circle*) and *Tollip*$^{-/-}$ (*black square*) mice after aerosol infection with 50-100cfu Mtb H37Rv strain.
160 N = 10 mice/group. $P < 0.0001$, Mantel-Cox test. **G)** Percentage of initial body weight after Mtb
161 aerosol infection *Circle* – WT mice; *square* - *Tollip*$^{-/-}$ mice. N = 10 / group. **H)** Hematoxylin and
162 eosin staining of Mtb-infected lung tissue from WT and *Tollip*$^{-/-}$ mice 4 and 8 weeks after aerosol
163 infection. **I)** Experimental outline of full bone marrow chimera experiments. **J)** Lung bacterial
164 burden of bone marrow chimeric mice, 8 weeks after aerosol Mtb infection. N = 5 mice/group.
165 * $p < 0.05$, ** $p < 0.01$, *** $p < 0.001$.
166
167 *TOLLIP deficiency induces increased intracellular Mtb burden in AM during chronic infection:*
168 Having shown that TOLLIP expression is required in hematopoietic cells for Mtb immunity, we
169 next sought to identify the specific hematopoietic cell types influenced by TOLLIP expression.
170 In prior studies, we showed that TOLLIP deficiency promotes diminished Mtb replication within
171 macrophages *in vitro*, which correlated with its role in diminishing proinflammatory cytokine
172 responses (*6, 30*). However, given the opposing results in both human genetic studies and
173 mouse infectious challenge, we investigated whether TOLLIP was required for Mtb control in
174 distinct pulmonary macrophages within the lung over the disease course. We infected *Tollip*$^{-/-}$

175 and WT mice with Mtb expressing an mCherry fluorescent reporter (50-100 CFU) via aerosol
176 and four and eight weeks after infection, we measured lung myeloid cell populations and the
177 proportion of cells infected with Mtb using an adaptation of recently devised gating strategies
178 (**Figure S2,** (*31, 32*)). We found no difference in the proportion of AM (CD11c+SiglecF+),
179 monocyte-derived macrophages (MDM; SiglecF-CD11b+CD11c+MHCII+), interstitial
180 macrophages (IM; SiglecF-CD11b+CD11c-MHCII+), neutrophils (PMN; SiglecF-CD11b+Ly6G+),
181 or dendritic cells (DC; SiglecF-CD11b-CD11c+MHCII+) found in the lung between WT and *Tollip*$^{-}$
182 $^{/-}$ mice during the course of Mtb infection (**Figure 2A-B**). When we assessed the infected cells,
183 however, we observed a lower percentage of mCherry+ AM and PMN infected with Mtb in
184 *Tollip*$^{-/-}$ mice, compared to WT mice four weeks post-infection (**Figure 2C**, $p = 0.01$ and $p = 0.02$,
185 respectively; $n = 5$). By eight weeks, however, there was a reversal and a significantly greater
186 proportion of Mtb-infected AM and MDM from *Tollip*$^{-/-}$ mice (**Figure 2D**, $p = 0.03$ and $p = 0.01$,
187 respectively). Thus, although the overall proportion of myeloid populations were similar in WT
188 and *Tollip*$^{-/-}$ mice, some myeloid cell subtypes, including AM, were relatively less infected at
189 early timepoints, and relatively more infected at later timepoints.

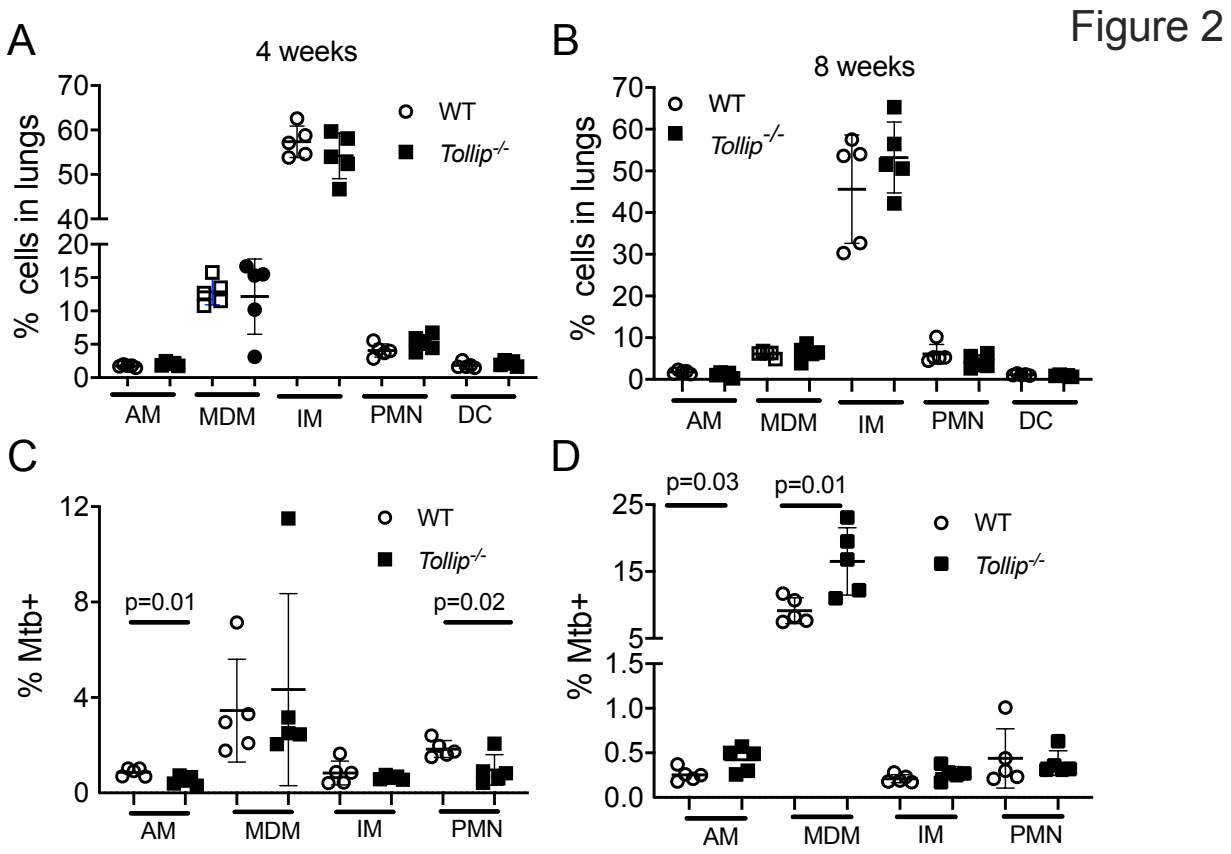

Figure 2. Mtb preferentially infects *Tollip*$^{-/-}$ myeloid cells 8 weeks after aerosol infection. Lungs from Mtb-infected mice were gently dissociated, and flow cytometry was performed. Gating strategy described in **Figure S2**. The proportion of lung resident myeloid cells from WT (*clear circle*) and *Tollip*$^{-/-}$ (*black square*) mice was compared **A)** 4 and **B)** 8 weeks after aerosol infection with 50-100 cfu mCherry-expressing Mtb. The proportion of each cell subset infected with Mtb (mCherry+) was compared between groups **C)** 4 and **D)** 8 weeks post infection. N = 5 mice/group. Experiment was performed three times independently. Statistical significance determined using Student's t-test. AM – alveolar macrophage, MDM – monocyte-derived macrophage, IM – interstitial macrophage, PMN – neutrophil, DC – dendritic cell.

201 *TOLLIP deficiency induces and maintains increased NOS2 expression in lung-resident myeloid cells*
202 *after Mtb infection*

203 Next, we compared the functional capacity of lung-resident myeloid cells in WT and
204 *Tollip*$^{-/-}$ mice. Four weeks post-infection, Mtb-infected AMs from *Tollip*$^{-/-}$ mice demonstrated
205 significantly increased NOS2 median fluorescence intensity when compared to WT littermates
206 (**Figure 3A**, p = 0.01, n = 5), and we observed a trend toward increased NOS2 from Mtb infected
207 PMNs in *Tollip*$^{-/-}$ mice. Eight weeks after infection, NOS2 expression was similar in all myeloid
208 cell types across WT and *Tollip*$^{-/-}$ mice (**Figure 3B**). We measured expression of MHC Class II and
209 CD80 between Mtb-infected and uninfected myeloid cells and found that, while MHC Class II
210 expression from each myeloid cell type was similar (data not shown), CD80 expression was
211 significantly diminished on Mtb-infected *Tollip*$^{-/-}$ AM (p = 0.008), MDM (p = 0.05), and PMN (p
212 =0.05) four weeks post-infection (**Figure 3C**, n = 5/group) and in *Tollip*$^{-/-}$ Mtb-infected AM and
213 MDM (**Figure 3D,** p=0.002 and p=0.004, respectively) eight weeks post-infection. In summary,
214 NOS2 expression, a marker associated with antimicrobial activity, was increased at early
215 timepoints in Mtb-infected AM, but this was not sustained at later timepoints. In contrast, CD80
216 expression, a molecule critical for T cell costimulation, was diminished at both early and late
217 timepoints in multiple Mtb-infected myeloid cell populations in *Tollip*$^{-/-}$ mice.

Figure 3

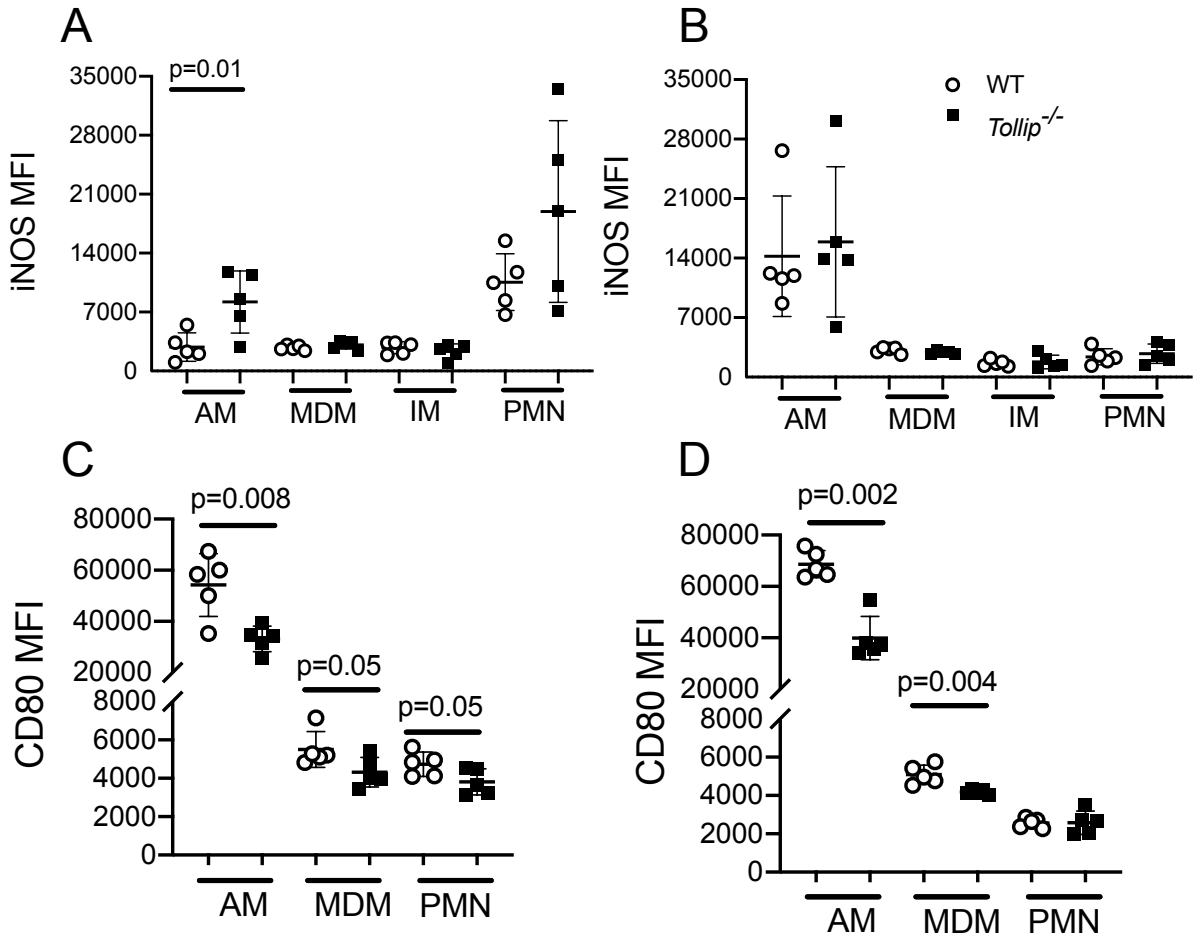

218

219 **Figure 3. *Tollip*$^{-/-}$ lung-resident myeloid cells develop enhanced antimicrobial responses**

220 **after Mtb infection.** Please see **Supplemental Figure 2** for gating strategy to identify myeloid

221 cell subsets. **A and B)** Intracellular NOS2 protein expression was measured in Mtb-infected

222 lung-resident myeloid cells (mCherry+) by flow cytometry **A)** 4 and **B)** 8 weeks post infection.

223 CD80 expression was measured **C)** 4 and **D)** 8 weeks post infection. Median fluorescence

224 intensity was compared using a two-sided t-test. N = 5 mice/group. WT (*clear circle*); *Tollip*$^{-/-}$

225 (*black square*). Experiment was repeated three times independently. AM – alveolar

226 macrophage, MDM – monocyte-derived macrophage, IM – interstitial macrophage, PMN –
227 neutrophil, DC – dendritic cell.
228
229 *Intrinsic expression of TOLLIP in AM regulates immunity against Mtb*
230 Our findings in Mtb-infected *Tollip*$^{-/-}$ mice suggested that TOLLIP expression in AM may
231 regulate their ability to control Mtb. However, in global *Tollip*$^{-/-}$ knockout mouse models, these
232 results could also reflect indirect effects of TOLLIP-deficiency in other cell types, or bacterial
233 burden differences between WT and *Tollip*$^{-/-}$ mice. To directly assess the intrinsic role of TOLLIP
234 in distinct myeloid populations, we generated mixed bone marrow chimeric mice by
235 combining bone marrow from F1 generation *WT* mice (CD45.1+CD45.2+) in a 1:1 ratio with
236 *Tollip*$^{-/-}$ (CD45.2+) bone marrow and transplanting this mix into CD45.1+ recipient mice (**Figure**
237 **4A**). After allowing 10 weeks for immune reconstitution and confirmation of equal proportions
238 of immune cells from each lineage (**Figure 4B**), we infected these mice with 50-100cfu Mtb-
239 mCherry and evaluated the induction and maintenance of the innate immune response to Mtb.
240 Our flow gating strategy is demonstrated in **Figure S3**. We recapitulated the pattern of early
241 innate immune responses to Mtb (*32*). 14 days after infection, AM were the primary cell
242 infected, but increasing proportions of PMN and MDM became infected over time, as described
243 in prior publications (**Figure 4C;** (*32*). We measured the proportion of *WT* and *Tollip*$^{-/-}$ myeloid
244 cells infected with Mtb over time. 14 days post infection, a greater percentage of *WT* AM were
245 infected with Mtb compared with *Tollip*$^{-/-}$ AM (**Figure 4D**, $p = 0.001$; paired t-test, $n = 5$,
246 representative of 3 independent experiments). In contrast, the percentage of Mtb-infected WT
247 and *Tollip*$^{-/-}$ MDM and PMN were similar. By d28, however, we observed a reversal of the AM
248 phenotype; a greater percentage of *Tollip*$^{-/-}$ AM were infected compared to their WT

249 counterparts (**Figure 4E**, p = 0.015). Further, despite the fact that AM make up a relatively
250 modest percentage of cells infected by Mtb, these cells are preferentially infected, suggesting
251 that they remain a preferential replicative niche throughout Mtb infection. A modest increase
252 in the proportion of Mtb-infected *Tollip*$^{-/-}$ PMN was also observed at d28 (**Figure 4E**, p = 0.02).
253 Consistent with our findings in global *Tollip*$^{-/-}$ mice, we found that NOS2 expression was
254 increased in *Tollip*$^{-/-}$ AM in the mixed chimeras as compared to WT AM (**Figure 4F**, p = 0.04;
255 paired t-test; n=5). Overall, these findings show a critical AM-intrinsic role for TOLLIP in the
256 regulation of their immune response to Mtb-infection and that the nature of this role changes
257 over time. At early timepoints, TOLLIP deficiency in AM restricts Mtb accumulation, however, at
258 later timepoints this is reversed and TOLLIP-deficiency in AM promotes cell-intrinsic Mtb
259 infection.

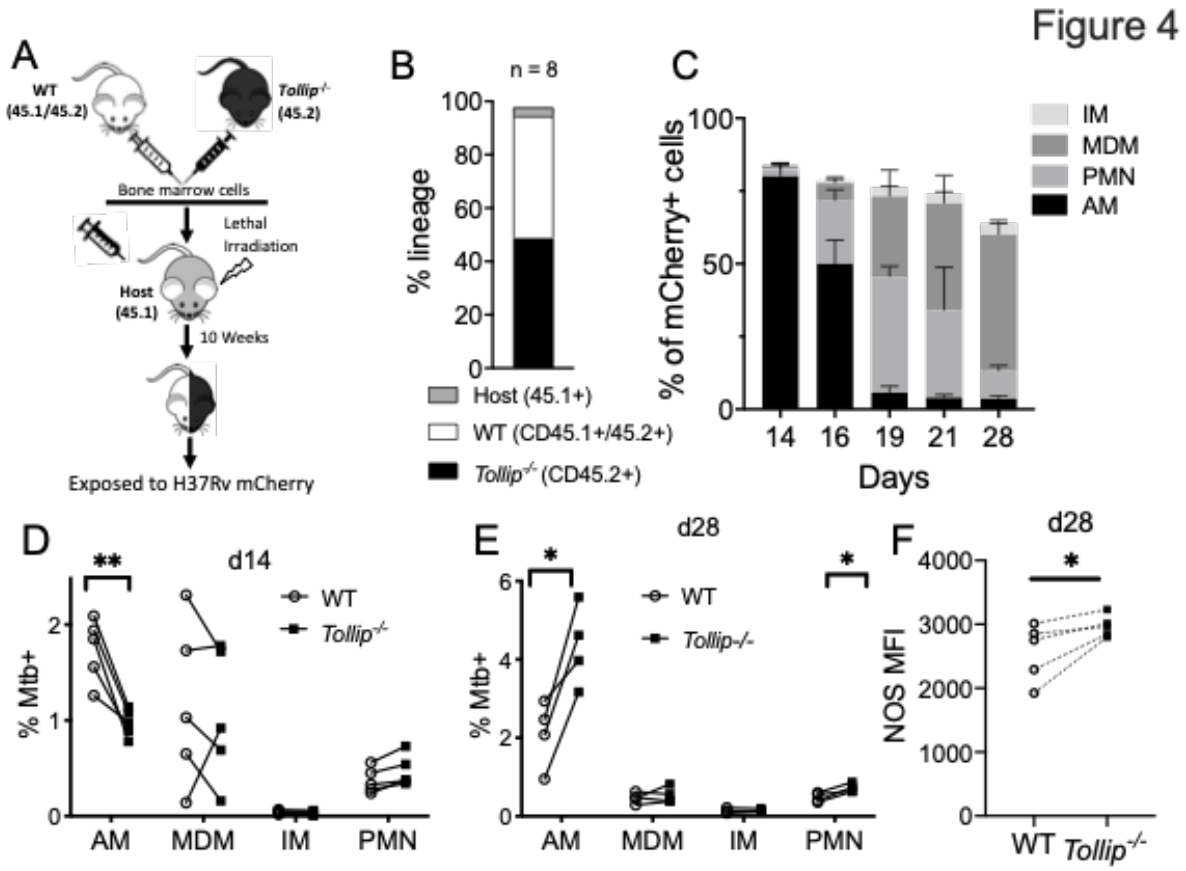

Figure 4. *Tollip*$^{-/-}$ AM become preferentially infected with Mtb over time. WT:*Tollip*$^{-/-}$ mixed bone marrow chimeric mice were infected with Mtb expressing mCherry (50-100 cfu) and followed. Gating strategy can be found in **Figure S3**. **A)** Experimental strategy and timeline. Mixed bone marrow chimeras were generated by mixing 1:1 ratios of WT (CD45.1+/CD45.2+) and *Tollip*$^{-/-}$ (CD45.2+) mice and transferred to a CD45.1+ murine host. **B)** Frequency distribution of CD45 expression in naïve mixed bone marrow chimeric mice. **C)** Composition of mCherry+ lung leukocytes at the indicated time point. **D and E)** Distribution of mCherry+ cells at **D)** d14 and **E)** d28 post-infection in mixed bone marrow chimeric mice. **F)** Median fluorescence intensity of nitric oxide synthase (NOS) in AM at d28 post-infection from mixed bone marrow chimeric mice. N = 4 or 5 mice for each time point as indicated; experiments were conducted

271 three times independently. * $p < 0.05$, ** $p < 0.005$. Significance determined by paired two-
272 sided t-test. AM – alveolar macrophage, MDM – monocyte-derived macrophage, IM –
273 interstitial macrophage, PMN – neutrophil.
274
275 Tollip$^{-/-}$ *AM develop increased EIF2 signaling responses after Mtb infection*
276 The early resistance of *Tollip*$^{-/-}$ AM to Mtb infection can be explained by the observation
277 that *Tollip*$^{-/-}$ macrophages exhibit elevated inflammatory responses and effector functions to
278 Mtb infection, but the reason Mtb persists within AM at later timepoints is less clear. Thus, we
279 evaluated the transcriptional networks associated with loss of Mtb control to identify alternate
280 TOLLIP mechanisms that alter AM function. We sorted infected and uninfected *Tollip*$^{-/-}$ and WT
281 AM from mixed bone marrow chimeric mice at d28 post-infection for analysis by RNA-Seq
282 (sorting strategy is shown in **Figure S4**). We identified 194 differentially expressed genes (DEG)
283 between WT and *Tollip*$^{-/-}$ Mtb-infected AM (**Figure 5A**; FDR < 0.05; gene names at **Table S2**,)
284 and 157 DEGs between WT and *Tollip*$^{-/-}$ Mtb-uninfected "bystander" AM using the same
285 stringent FDR criteria. (**Figure 5B;** list in **Table S2**). The full gene list is available at
286 https://github.com/altman-lab/JS20.01**.** We investigated genotype-specific gene sets in each
287 group by applying weighted gene coexpression network analysis (WGCNA) and comparing
288 Mtb-infected or -uninfected "bystander" AM by TOLLIP genotype. We used supervised-WGCNA,
289 first identifying and subsetting to 3899 DEGs that met a more lenient FDR cutoff < 0.3
290 comparing among the 4 groups, to identify 17 distinct coexpression modules containing 54-
291 583 genes per module (**Table S3**). The average expression of genes in each module was then
292 modeled comparing the two AM subsets (WT vs *Tollip*$^{-/-}$) in each condition (infected or
293 uninfected; **Figure 5C**). To understand the biological function of the genes within each module,

294 we tested for enrichment of genes in the curated Broad Institute MSigDB Hallmark gene sets,
295 which represent well-defined biological states and processes that display coherent expression
296 (*33*). Multiple pathways were enriched in each module, as visualized by percent of genes in
297 each module that map to Hallmark terms significant for at least one model (FDR < 0.05; **Figure**
298 **5D, Table S4**). Inflammatory/immune pathways (IFNγ response, TNFα signaling via NF-kB,
299 inflammatory response, and IL2/STAT5 signaling) were enriched in modules with decreased
300 expression in *Tollip*$^{-/-}$ AM, consistent with the prior observation that TOLLIP increases
301 inflammation due to post-translational trafficking of immune receptors. Thus, decreased
302 transcript here is consistent with transcriptional feedback loops to this activity and expected,
303 based on experimental data regarding TOLLIP's mechanism of action (*1*). By contrast, the
304 unfolded protein response, adipogenesis, mTORC1 signaling, oxidative phosphorylation, and
305 fatty acid metabolism were enriched in modules with increased expression in *Tollip*$^{-/-}$ AM.

306 To summarize the functional interpretations of RNA sequencing results, we merged
307 modules into 6 subgroups according to a specific pattern of either significantly increased or
308 decreased expression in *Tollip*$^{-/-}$ vs WT AM from 1) Mtb-infected AM only, 2) Mtb-uninfected
309 bystander AM only, or 3) both Mtb-infected and -uninfected populations. We similarly
310 evaluated for pathway enrichment in Hallmark gene sets. The modules showing increased
311 gene expression in *Tollip*$^{-/-}$ Mtb-infected cells were significantly enriched with oxidative
312 phosphorylation (FDR q = 3.96×10^{-56}), adipogenesis (q = 2.46×10^{-13}), MTORC1 signaling (q =
313 1.95×10^{-10}), fatty acid metabolism (q = 2.52×10^{-7}), and unfolded protein response (q = 9.33×10^{-6};
314 **Figure 5E**). The modules showing decreased expression from both Mtb-infected and bystander
315 populations were significantly enriched for hypoxia (q = 1.93×10^{-11}) and glycolysis (q = $1.12 \times 10^{-}$

316 ^{8}), mitotic spindle (q = 1.93×10^{-19}) and G2M checkpoint (q = 1.03×10^{-6}), both cell cycle
317 transcriptional programs, and allograft rejection (q = 1.93×10^{-11}), inflammatory response (q =
318 1.93×10^{-11}), IL-2/STAT5 signaling (q = 1.12×10^{-8}), IFN-γ response (q = 1.12×10^{-8}; **Figure 5F**), which
319 are consistent with multiple immune and inflammatory signaling pathways. The other groups
320 did not demonstrate any significant enrichment for Hallmark gene sets. We performed
321 Ingenuity Causal Network Analysis on genes enriched in Mtb-infected AM (FDR q < 0.05) to
322 identify the upstream regulatory pathways responsible for the observed effects in Mtb-infected
323 *Tollip*$^{-/-}$ AM. We found that the strongest association with increased EIF2 Signaling pathway
324 (**Figure 5G**; z-score 2.714, p = 2.71×10^{-9}), EIF2 complex signaling as the primary responsible
325 upstream pathway for phenotypes observed in **Figure 5E**, among Mtb-infected AM.

Figure 5

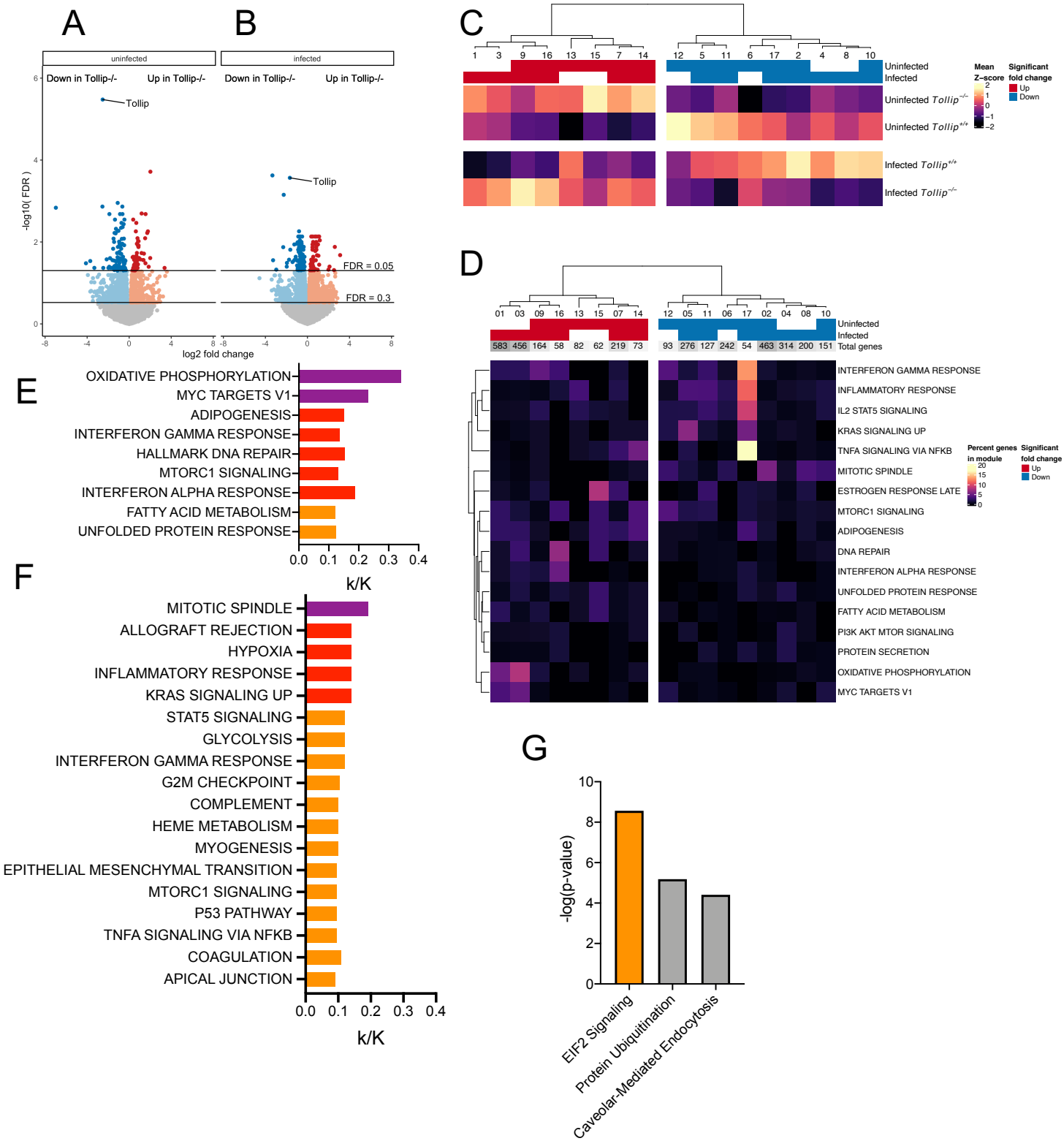
A
B
uninfected
infected
Down in Tollip-/-
Up in Tollip-/-
Tollip
FDR = 0.05
FDR = 0.3
-log10(FDR)
log2 fold change
C
Uninfected
Infected
Uninfected Tollip-/-
Uninfected Tollip+/+
Infected Tollip+/+
Infected Tollip-/-
Mean Z-score
Significant fold change
Up
Down
D
Uninfected
Infected
Total genes
INTERFERON GAMMA RESPONSE
INFLAMMATORY RESPONSE
IL2 STAT5 SIGNALING
KRAS SIGNALING UP
TNFA SIGNALING VIA NFKB
MITOTIC SPINDLE
ESTROGEN RESPONSE LATE
MTORC1 SIGNALING
ADIPOGENESIS
DNA REPAIR
INTERFERON ALPHA RESPONSE
UNFOLDED PROTEIN RESPONSE
FATTY ACID METABOLISM
PI3K AKT MTOR SIGNALING
PROTEIN SECRETION
OXIDATIVE PHOSPHORYLATION
MYC TARGETS V1
Percent genes in module
E
OXIDATIVE PHOSPHORYLATION
MYC TARGETS V1
ADIPOGENESIS
INTERFERON GAMMA RESPONSE
HALLMARK DNA REPAIR
MTORC1 SIGNALING
INTERFERON ALPHA RESPONSE
FATTY ACID METABOLISM
UNFOLDED PROTEIN RESPONSE
k/K
F
MITOTIC SPINDLE
ALLOGRAFT REJECTION
HYPOXIA
INFLAMMATORY RESPONSE
KRAS SIGNALING UP
STAT5 SIGNALING
GLYCOLYSIS
INTERFERON GAMMA RESPONSE
G2M CHECKPOINT
COMPLEMENT
HEME METABOLISM
MYOGENESIS
EPITHELIAL MESENCHYMAL TRANSITION
MTORC1 SIGNALING
P53 PATHWAY
TNFA SIGNALING VIA NFKB
COAGULATION
APICAL JUNCTION
k/K
G
-log(p-value)
EIF2 Signaling
Protein Ubiquitination
Caveolar-Mediated Endocytosis

326

327

328 **Figure 5. Global gene expression analysis of Mtb-infected *Tollip*$^{-/-}$ AM 28 days after**

329 **infection demonstrates increased EIF2 signaling.** Mixed bone marrow chimeric mice were

330 infected with mCherry-expressing Mtb and 28 days after infection, Mtb-infected and Mtb-

331 uninfected WT and *Tollip*$^{-/-}$ AM were sorted and RNA-seq was performed. Sorting strategy can

332 be found in **Figure S3**. **A)** Volcano plot of gene expression (log2 fold change) and significance

333 (-log10(FDR)) for genes between *Tollip*$^{-/-}$ (CD45.2) and WT (CD45.1+CD45.2+), Mtb-uninfected

334 and **B)** Mtb-infected AMs. Horizontal lines indicate significant genes (FDR < 0.05) and genes

335 used in WGCNA modules (FDR < 0.3) **C)** Heatmap of mean module z-score for infection:

336 TOLLIP groups. Red bars indicate increased expression in *Tollip*$^{-/-}$ AM and blue bars indicated

337 decreased expression in *Tollip*$^{-/-}$ AM, separated by infection status. Modules (columns) were

338 average hierarchical clustered. **D)** Heat map of enrichment of significant Hallmark gene sets

339 (FDR q-value < 0.05) in modules. Color indicates percent of genes in a module that mapped to

340 a given Hallmark. The total number of genes in each module is indicated above. Modules

341 (columns) were clustered as in **C)** and Hallmark terms (rows) were average hierarchical

342 clustered based on enrichment percentages. Red and blue bars are as in **C)**. **E-F)** Bar graph of

343 the Hallmark terms enriched in modules with **E)** increased expression in Mtb-infected, *Tollip*$^{-/-}$

344 AM or **F)** decreased expression in both Mtb-infected and bystander AM. Bar length indicates

345 the proportional enrichment of each pathway. Color indicates degree of significance: *purple* –

346 FDR q < 10^{-16}; *red* -- q < 10^{-8}; *orange* – q < 10^{-4}. **G)** Ingenuity Pathway Analysis of upstream

347 regulatory pathways enriched by data for Mtb-infected cells. *Orange* bar indicates increased

348 expression in *Tollip*$^{-/-}$ AM. *Gray* bars indicate no directional data available.

349

350 *Lipid accumulation in* Tollip$^{-/-}$ *AM permits intracellular Mtb replication*

351 Bioinformatic analysis suggests that EIF2 signaling, a master switch for the cellular stress
352 response, is the upstream pathway with the strongest association with *Tollip*$^{-/-}$ Mtb-infected AM
353 during chronic Mtb infection. Given the observation of increased foam cells in *Tollip*$^{-/-}$ mice after
354 Mtb infection, we hypothesized that macrophages lacking TOLLIP accumulated excess lipid,
355 which induced EIF2, followed by and maladaptive responses to Mtb. During lipid excess,
356 autophagy and proteosomal activity are induced to control lipid droplet (LD) accumulation
357 (*34*). We first tested the capacity of *Tollip*$^{-/-}$ macrophages to perform bulk macroautophagy in
358 bone marrow derived macrophages (BMDMs) of WT or *Tollip*$^{-/-}$ mice by measuring protein levels
359 of LC3II and p62. To evaluate flux through autophagy, we treated BMDMs with the vATPase
360 inhibitor Bafilomycin A (BafA), which prevents autophagosome/lysosome fusion. As expected,
361 levels of the autophagosome protein marker LC3II were significantly upregulated following
362 BafA treatment. Notably, *Tollip* deletion did not significantly affect levels of LC3II, nor the
363 induction of LC3II by BafA treatment (**Figures 6A-B**). We also assessed levels of the adaptor
364 protein p62, which both targets cargo to autophagosomes for clearance and is itself cleared
365 during autophagy. We again observed similar levels of p62 in both groups, without significant
366 differences in the rise of p62 following BafA treatment (**Figures 6B-C**). However, we did note a
367 non-significant trend towards increased BafA-induced p62 accumulation in *Tollip*$^{-/-}$ cells that
368 could reflect compensation for Tollip deficiency given analogous roles for the proteins (*2, 30*).
369 Nonetheless, these studies indicate that TOLLIP is dispensable for macroautophagy and
370 autophagic flux in macrophages. We also evaluated the impact of TOLLIP on selective
371 autophagy of Mtb within macrophages. We infected TOLLIP-deficient and control macrophage
372 cell lines, regularly used in our lab (*6*), with Mtb expressing mCherry and found no differences

373 between these groups in the proportion of Mtb colocalizing to LC3+ autophagosomes (**Figure**
374 **S5**).

375 We then evaluated the capacity for TOLLIP to promote lipid clearance overall. We
376 incubated WT and *Tollip*$^{-/-}$ PEM with the mycobacterial cell wall product mycolic acid (MA;
377 10mg/ml) for 72 hours, stained with fluorescent dye against neutral lipid, and measured the
378 number of LD per cell by microscopy. *Tollip*$^{-/-}$ PEM displayed significantly increased numbers of
379 LD/cell (**Figure 6D**). We noted no difference in the proportion of PEM with quantifiable LD,
380 indicating equal lipid uptake between cells (**Figure 6E**), but a significant increase in the number
381 of LD in *Tollip*$^{-/-}$ PEM (**Figure 6F**, $p = 0.02$). Next, we evaluated if lung macrophages
382 demonstrated this effect as well. We stained single cell suspensions from the lungs of mixed
383 bone marrow chimeric mice at d28 post-infection for neutral lipid, using gating described in
384 **Figure S4**. We found that *Tollip*$^{-/-}$ AM accumulated significantly more lipid *in vivo* than WT AM,
385 irrespective of their infection with Mtb, while MDM did not significantly accumulate
386 intracellular lipid (**Figure 6G**, $p = 0.03$; $n = 5$). A representative histogram for lipid accumulation
387 in AM and MDM is displayed (**Figure 6H**; WT AM – *blue*; *Tollip*$^{-/-}$ AM – *red*).

388 We measured the impact of lipid accumulation on stress signal transduction and
389 intracellular Mtb replication. First, we confirmed that MA is associated with increased stress
390 responses from BMDM after Mtb infection. In both WT and *Tollip*$^{-/-}$ BMDM, canonical stress
391 signal transduction transcript expression is stable or decreased 24hr after Mtb infection. In WT
392 BMDM, the addition of excess MA does not influence this expression and Tollip-/- BMDM
393 demonstrate decreases in expression after infection. However, after exposure to excess MA,
394 followed by overnight live Mtb infection, *Ern1* (**Figure S6A**, $p = 0.0007$) , *Eif2ak3* (**Figure S6B**, p
395 $= 0.004$), and *Atf6* expression (**Figure S6C**, $p = 0.04$) is significantly and selectively increased in

396 *Tollip*$^{-/-}$ cells. (**Figure S6A-C**) We infected WT and *Tollip*$^{-/-}$ PEM with a luminescent strain of Mtb
397 H37Rv (Mtb-*lux*, MOI 1; gift of Jeffrey Cox), incubated with or without MA or BSA-conjugated
398 peptidoglycan (PG-BSA) as a non-lipid control. *Tollip*$^{-/-}$ PEM incubated with MA (**Figure 6I**, p =
399 0.023-way ANOVA accounting for TOLLIP and MA) demonstrated increased Mtb replication
400 compared with *Tollip*$^{-/-}$ PEM in the absence of excess lipid or lipid-incubated WT PEM. Taken
401 together, these results show that TOLLIP prevents lipid accumulation within AM, which induces
402 ER stress, and that dysregulation of the ER stress during chronic infection promotes intracellular
403 Mtb persistence and replication.
404

Figure 6

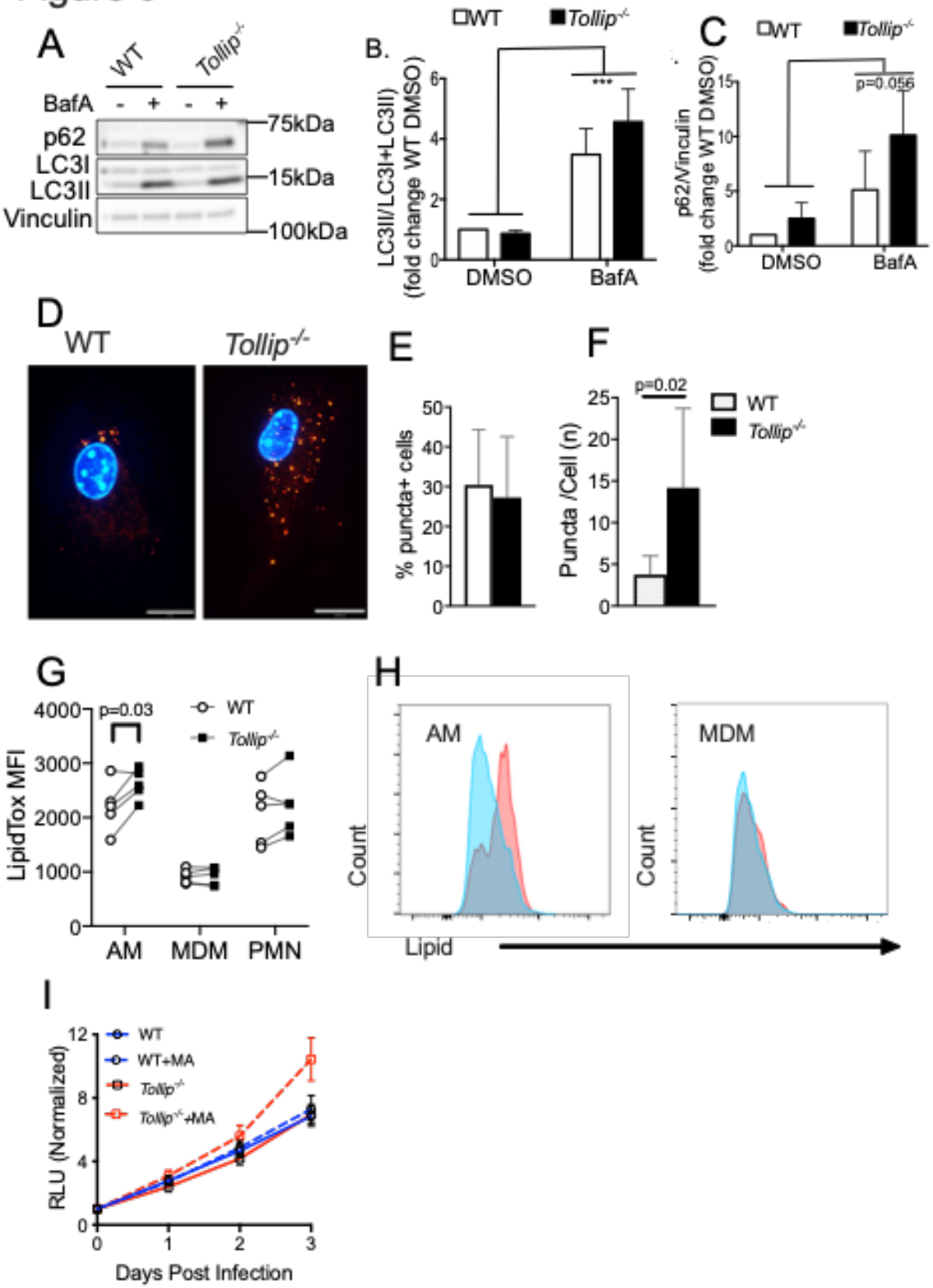
A
WT
Tollip-/-
BafA
- + - +
p62
LC3I
LC3II
Vinculin
75kDa
15kDa
100kDa
B.
WT
Tollip-/-
LC3II/(LC3I+LC3II)
(fold change WT DMSO)
***
DMSO
BafA
C
WT
Tollip-/-
p62/Vinculin
(fold change WT DMSO)
p=0.056
DMSO
BafA
D
WT
Tollip-/-
E
% puncta+ cells
F
p=0.02
WT
Tollip-/-
Puncta /Cell (n)
G
p=0.03
WT
Tollip-/-
LipidTox MFI
AM
MDM
PMN
H
AM
MDM
Count
Lipid
I
WT
WT+MA
Tollip-/-
Tollip-/-+MA
RLU (Normalized)
Days Post Infection

405

406 **Figure 6. *Tollip*$^{-/-}$ AM accumulate excess lipid that creates a permissive environment for**
407 **Mtb replication.** Bone marrow from WT (*black bars*) or *Tollip*$^{-/-}$ (*white bars*) were differentiated
408 *ex vivo* to macrophages using 40ng/mL mCSF for 7-9 days. Following differentiation, BMDMs
409 were treated for 6hr with or without 250nM Bafilomycin A (BafA). **A**) Representative western
410 blot results showing protein levels of LC3I/II and p62. **B**) Quantification of protein levels (by
411 densitometry) of LC3II using total LC3 (I+II) as a loading control. ***$p<0.001$ 2-way ANOVA for
412 an effect of BafA **C**) Quantification of p62 levels (by densitometry) using vinculin as a loading
413 control. $p=0.056$ 2-way ANOVA effect of BafA. **D-F**) WT and *Tollip*$^{-/-}$ peritoneal exudate
414 macrophages (PEM) were isolated and incubated with mixed mycolic acids (MA) for 72hrs.
415 PEM were stained with LipidTOX Red dye (*red*) and DAPI (*blue*), fixed, and visualized with
416 fluorescent microscopy. **D)** Representative image for of lipid droplet (LD) accumulation in WT
417 and *Tollip*$^{-/-}$ PEM. **E)** Percentage of cells with visible LD, of 100 cells imaged. Bar – error bars
418 (mean ± SD). **F)** Total number of LD per cell, of 100 cells with detectable LD. Bar – error bars
419 (mean ± SD). **G)** Median fluorescence intensity of alveolar macrophages (AM) and monocyte-
420 derived macrophages (MDM) stained with LipidTox neutral lipid stain from mixed bone
421 marrow chimeric mice 28 days after Mtb infection. Infection and gating were performed as in
422 **Figure 5**. Lines connect WT and *Tollip*$^{-/-}$ AM from the same mouse. Significance calculated
423 using two-sided paired t-test. **H)** Representative histogram of AM and MDM lipid staining
424 from one experiment (WT – blue; *Tollip*$^{-/-}$ – red). **I** Luminescence over time in WT and *Tollip*$^{-/-}$
425 PEM's incubated with exogenous lipid - MA, mycolic acid (10µg/ml) and infected with Mtb
426 H37Rv expressing *lux* luminescence gene (MOI 1). PEMs were isolated and incubated with MA
427 for 72 hr before infection. Intracellular replication was measured by luminescence for each
428 group over the next three days in quadruplicate and repeated three times to assess

429 reproducibility. Statistical significance was determined by 3-way ANOVA accounting for time,
430 genotype, and lipid administration.
431
432 *EIF2 Signaling Permits Mtb Replication in Macrophages*
433 After determining that TOLLIP permitted lipid accumulation, which induced cellular
434 stress, we next evaluated the impact of EIF2 activation directly on intracellular Mtb replication.
435 EIF2 is required for protein translation and either complete knockout or activation of this
436 pathway is lethal (*35*). Therefore, we measured effects of this pathway with raphin-1 treatment,
437 a novel inhibitor of protein phosphatase-1, that effectively enhances EIF2 phosphorylation and
438 activation without inducing cell death (*36*). Raphin-1 treatment had no effect on cell death in
439 uninfected macrophages, nor did it influence Mtb replication in broth culture (data not shown).
440 We treated WT PEM with raphin-1 (10μM) or control, then infected these cells with Mtb-*lux* (MOI
441 1) and followed luminescence over time. Raphin-1 treatment increased Mtb replication in WT
442 PEM (**Figure 7A**; p = 0.0002, 2-way ANOVA accounting for time and treatment). As
443 demonstrated previously, MA alone did not increase Mtb replication in WT PEM, but raphin-1
444 treatment increased Mtb replication, without evidence of any additive effect with cotreatment
445 with MA and raphin-1 together (**Figure 7B**). Raphin-1 treatment of *Tollip*$^{-/-}$ PEM was associated
446 with increased Mtb replication in *Tollip*$^{-/-}$ PEM compared with WT PEM (**Figure 7C**, p = 0.0475,
447 3-way ANOVA accounting for TOLLIP, raphin-1, and time). We treated *Tollip*$^{-/-}$ PEM with MA,
448 which was associated with increased impaired Mtb luminescence compared with PEM 72 hr
449 after infection (**Figure 7D**; p = 0.0147, two-sided t-test). Raphin-1 treatment of *Tollip*$^{-/-}$ PEM
450 induced further increases in Mtb replication above MA (**Figure 7D**, p = 0.12). MA and raphin-1
451 treatment together in *Tollip*$^{-/-}$ PEM induced no synergistic increases in replication, compared

452 with MA alone, after 72 hr (**Figure 7D**). These data demonstrate that EIF2 signaling permits
453 increased Mtb growth, and that decreased TOLLIP expression increases the potency of raphin-
454 1 toward Mtb replication within macrophages.
455

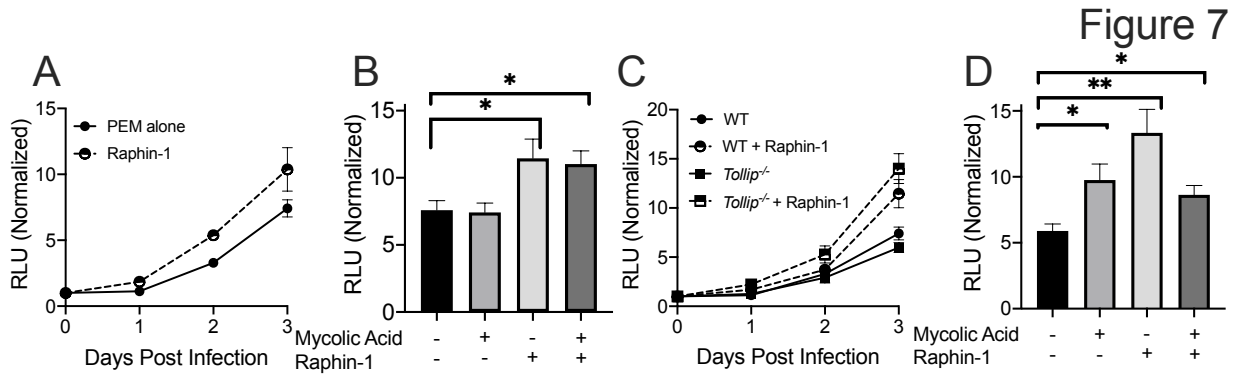

456

457 **Figure 7. EIF2 Activation Impairs Mtb Control in Macrophages.** Peritoneal extract
458 macrophages (PEM) were plated and infected with Mtb expressing the lux luminescence
459 plasmid (MOI 1). For each experiment luminescence was measured at the time points
460 described. A) WT PEM were treated with vehicle control or raphin-1 (10μM) at the time of
461 infection. Luminescence was measured over time. Statistical significance determined by 2-
462 way ANOVA accounting for time and treatment. B) WT PEM were treated with mycolic acid
463 (MA; 10μg/ml) for 72hr, then treated with either vector control or raphin-1 at the time of Mtb
464 infection. Bars represent luminescence at 72hr after infection. Statistical significance
465 determined by 2-way t-test. C) WT and *Tollip*$^{-/-}$ PEM were treated with vehicle control or
466 raphin-1, infected with Mtb, then luminescence was measured over time. Statistical
467 significance determined by 3-way ANOVA accounting for TOLLIP expression, time, and
468 treatment. D) *Tollip*$^{-/-}$ PEM were treated with MA, raphin-1, or vehicle control as in B).
469 Luminescence was measured 72h after infection. Statistical significance determined by two-

470 sided unpaired t-test. Experiments were performed six times, all data is shown. * $p < 0.05$, ** p
471 < 0.01.
472
473 *EIF2 Signaling Complex Proteins are Enriched in Human TB Granulomas*
474 A defining characteristic of human granulomas is the presence of "caseum," a lipid-rich
475 center of necrosis (*37*). This central area of necrosis is surrounded by foam cells and other
476 inflammatory cells induced by Mtb infection(*38*). Because we found that EIF2 signaling was
477 induced by lipid accumulation and permissive to Mtb growth, we hypothesized that EIF2
478 complex genes are enriched in caseous granulomas. EIF2 signaling is activated by the
479 phosphorylation of *EIF2S1*, at Ser48 and Ser51 by one of four upstream kinases which are
480 responsive to different stress stimuli – *EIF2AK1* (HRI; heavy metals), *EIF2AK2* (PKR; dsRNA),
481 *EIF2AK3* (PERK; unfolded protein/lipid), and *EIF2AK4* (GCN2; nutrient stress)(*13*). We evaluated
482 the gene expression of *EIF2S1* and its four upstream kinases in human caseous granulomas (*16*).
483 We compared mRNA transcript expression in lung tissues isolated from the caseous
484 granulomas of individuals infected with TB with samples from healthy areas of the same lungs
485 (n = 7 total). *EIF2AK1* (**Figure 8A**; FDR = 0.011), *EIF2AK2* (**Figure 8B**, FDR = 0.016), and *EIF2AK3*
486 (**Figure 8C**, FDR = 0.002) demonstrated significantly increased expression in caseous
487 granulomas. We did not detect significant increases in *EIF2S1* **(Figure 8D**). *EIF2AK4* and *TOLLIP*
488 expression were also increased in TB granulomas (**Figure 8E-F**; FDR = 0.25 and 0.08,
489 respectively), but did not meet our strict criteria for achieving statistical significance.
490

Figure 8

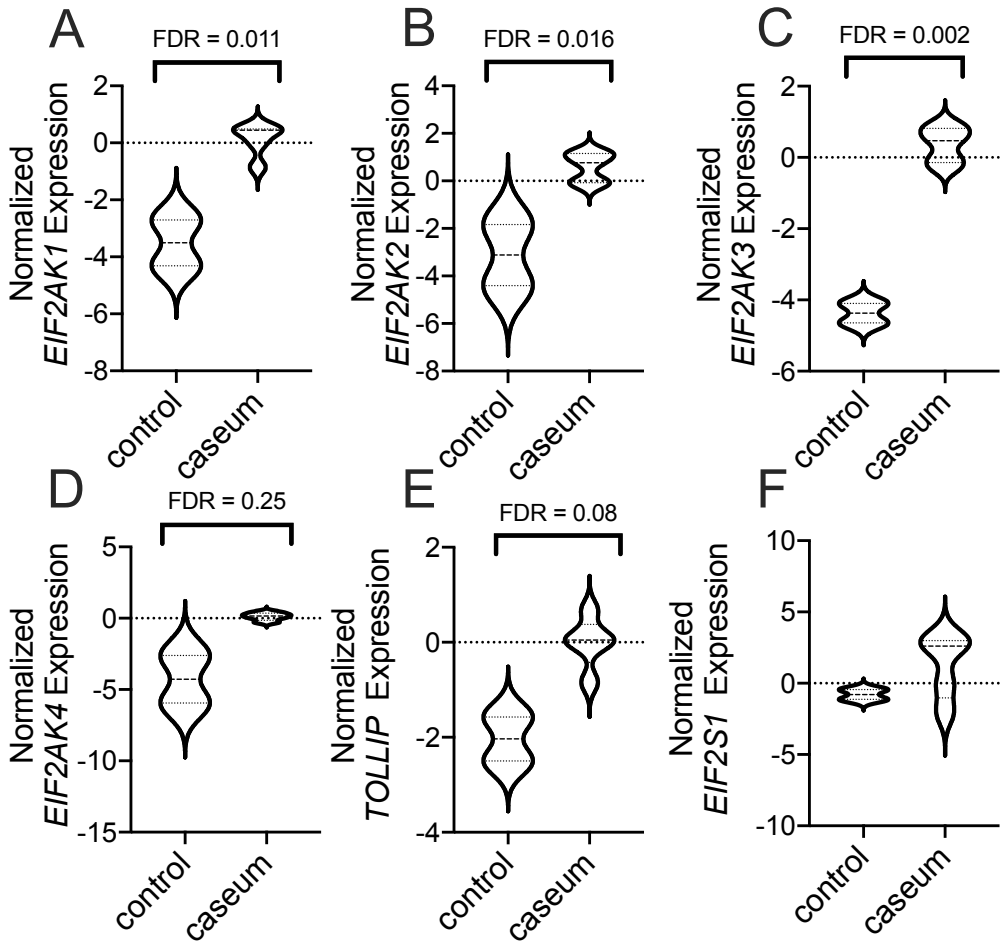

Figure 8. EIF2 Kinases are Enriched in Caseous TB Granulomas. Expression of A) *EIF2AK1*, B) *EIF2AK2*, C) *EIF2AK3*, D) *EIF2AK4*, E) *EIF2S1*, *and* F) *TOLLIP* in human caseous granuloma tissue, compared with healthy appearing lung tissue from different lobes from the same individuals. N = 7. Data are derived from the analysis of the publicly available GEO dataset GSE20050 using the indicated probe sets. FDR – false discovery rate. FDR is indicated above each data point.

Discussion

500 Although intracellular lipid accumulation is a consistent feature of Mtb infection in
501 humans, its relative absence in small animal models makes study of these phenotypes
502 challenging. Mice lacking *Tollip* develop excessive lipid accumulation while maintaining
503 increased innate immune activation. Therefore, this model of lipid accumulation is useful to
504 evaluate excess lipid influences Mtb pathogenesis during prolonged infection and to define
505 the molecular pathways responsible for these observed phenotypes. Computational analysis
506 of lipid-loaded, Mtb-infected *Tollip*$^{-/-}$ AM revealed that EIF2 signaling was the upstream
507 pathway responsible for increased Mtb persistence, suggesting an important contribution of
508 the ISR on Mtb pathogenesis *in vivo*. Importantly, lipids alone are sufficient to induce
509 intracellular lipid accumulation and stress selectively in *Tollip*$^{-/-}$ macrophages. Further, EIF2
510 kinases are enriched in human granulomas, providing human context for this observation.
511
512 EIF2 signaling prevents effective macrophage control of Mtb. ER stress complex
513 proteins are increased in murine lungs after Mtb infection (*25*), but whether they are beneficial
514 or harmful to the host has been challenging to determine previously (*16, 39*). Low level, acute
515 EIF2 activity inhibits protein translation, except for a suite of proteins induced to maintain
516 cellular survival, primarily through ATF4. ATF4 inhibits glycolysis and induces oxidative
517 phosphorylation, (*40*) a metabolic pattern that is maladaptive in the Mtb-infected lung, and
518 severe or prolonged EIF2 activation induces cellular death via CHOP (*41*). In a stressed state
519 such as a caseous granuloma, all cells may die from stress in the necrotic center. Moreover,
520 thresholds for cell death in response to stress are cell-specific, as secretory cells, such as plasma
521 cells and islet cells, are more sensitive to stress (PMID 28951826;). Bringing these two
522 observations together, the structure of human granulomas may be at least in part dictated by

523 EIF2-induced stress responses, as they are classically lipid-rich, contain a central area of lipid
524 necrosis, surrounded by foamy macrophages, then epithelioid macrophages and T and B cells.
525 These data suggest a geographic and environmental gradient of ER stress signals contribute to
526 necrosis, cellular distribution and morphology, and influence immune dysfunction and Mtb
527 progression. Our study demonstrates that on balance, EIF2 signaling induced by lipid excess is
528 maladaptive for Mtb control. Understanding how EIF2 signals impact granuloma formation
529 may provide tools for improving the immune responses to Mtb.
530
531 How excess lipid induces stress to permit Mtb persistence within macrophages is not
532 well described. In other cells, fatty acids induce cellular toxicity after destabilizing lysosomal
533 membranes and increasing their permeability (*42*). Acid sphingomyelinase, a lysosomal
534 enzyme, is required to cleave ceramide to sphingosine, which specifically induces lysosomal
535 permeability (*43*). Permeability depletes calcium within the ER, which leads to mitochondrial
536 oxidative stress (*44*). In settings of lysosomal permeability, cathepsins and other components
537 of toxic granules may cross into the cytoplasm and induce macrophage necrosis and further
538 exacerbate cellular stress. (*45, 46*). Recent zebrafish studies demonstrate that ER calcium flux
539 and reactive oxygen species determine Mtb-induced macrophage cell death and Mtb escape
540 from the macrophage (*21*). In Mtb-infected *Tollip*$^{-/-}$ AM, we note strong enrichment of
541 sphingolipid metabolic pathways. Combined with the observation that TOLLIP prevents lipid
542 accumulation, we surmise that TOLLIP-deficient macrophages accumulate excess sphingosine
543 to create lysosomal permeability and induce EIF2 signaling to permit Mtb replication. EIF2 then
544 induces downstream cell cycle arrest and impaired metabolic adaptation, which provide a
545 replicative niche for Mtb despite increasing inflammation in the surrounding tissues

546

547 In mixed bone marrow chimeras, *Tollip*$^{-/-}$ AM developed increased Mtb burden 28 days
548 post-infection. However, full knockout mice developed increased bacterial burden eight weeks
549 post-infection. The reason for this observed difference is uncertain. Chimeric mice undergo full
550 body radiation and bone marrow transplant, and this disruption of the bone marrow impacts
551 future immune responses, including influencing the immune response to pathogens.
552 Decreased TOLLIP expression is associated with impaired lung transplant engraftment, and so
553 TOLLIP deficiency may selectively influence the immune response to mycobacteria after bone
554 marrow reconstitution (*47*). However, we identified these phenotypes within multiple mouse
555 models, and find this phenotype recapitulated in genetic studies of TOLLIP (*6, 28*). Alternately,
556 intracellular carriage of mycobacteria within AM may more sensitively measure mycobacterial
557 burden than total lung Mtb bacterial CFU, as intracellular replication within AM may precede
558 replication in the lung overall. Thus, our observations in AMs using mixed bone marrow
559 chimeric mice may represent a "leading indicator" toward the chronic, maladaptive phenotype.
560 We focused on the impact of TOLLIP on macrophage biology in this study and discovered that
561 it plays an AM-intrinsic role in lipid clearance, but TOLLIP is ubiquitously expressed and may
562 influence the function of multiple immune cell subsets. Selective autophagy receptors alter
563 dendritic cell function, particularly during EBV, influenza, yellow fever vaccine, and *L.*
564 *monocytogenes* infection (*48-50*). ER stress response protein XBP1 prevents dendritic cell
565 apoptosis and permits T cell activation during lipid excess in ovarian cancer models (*22*). TOLLIP
566 may also impact T cell activation and differentiation. Another selective autophagy receptor,
567 TAX1BP1, permits T cells to meet the energy demands of activation and proliferation (*51*), and
568 autophagy supports regulatory T cell lineage stability by maintaining its metabolic

569 homeostasis (*52*). Thus, TOLLIP may influence autophagy and cellular homeostasis, and lipids
570 may impact cellular function, across cell types during Mtb infection.
571
572 Studies from the preantibiotic era regularly describe "post-primary" tuberculosis as an
573 acute, paucibacillary, caseating lipoid pneumonia obstructing bronchioles in a "tree-in-bud"
574 pattern (*53-55*), but its impact on Mtb pathogenesis is not clearly defined (*38*). In contrast, the
575 classically defined cavitating granuloma is strongly associated with chronic established Mtb
576 disease. Within this lipoid pneumonia, obstructed alveoli attract macrophages with a foamy
577 appearance, leading to subsequent lipoid necrosis and granuloma formation around caseous
578 necrosis. Pathologically, this obstructive lipoid pneumonia precedes the transition from
579 asymptomatic to symptomatic TB disease (*38*). Thus, a combination of genetic factors that
580 influence lipid clearance and physical factors that obstruct clearance of lipid debris may set
581 the stage for progressive TB disease. Providing means to 1) promote ongoing lipid clearance
582 or 2) relieve bronchial obstruction during the earliest phases of Mtb infection may prevent TB
583 progression from early silent infection to symptomatic disease. Further, therapies to prevent
584 this phenotype or resolve it may sensitize macrophages to immune signals, improving the
585 effectiveness of vaccine candidates. Preventing lipid-induced EIF2 signaling via TOLLIP may
586 be an effective host directed therapeutic strategy.
587
588 **Materials and Methods:**
589 *Reagents*
590 A complete list of reagents can be found in **Table S1**.
591

592 *Mice*

593 All mice were housed and maintained in specific pathogen-free conditions at the University of
594 Washington and Seattle Children's Research Institute, and all experiments were performed in
595 compliance with the Institutional Animal Care and Use Committee from each institution. Mice
596 used in the experiments were 6-12 weeks of age. B6.Cg-Tollip^{tm1Kbns}/Cnrm (*Tollip*$^{-/-}$) mice were
597 obtained from the European Mutant Mouse Archive (www.infrafrontier.eu) (*56*). Mice were
598 backcrossed 11 times on C57BL/6J background and were confirmed to be >99% C57BL/6J
599 genetically by screening 150 SNP ancestry informative markers (Jax, Inc). Genotyping was
600 performed using DNA primers for neomycin (Forward sequence: AGG ATC TCC TGT CAT CTC
601 ACC TTG CTC CTG; Reverse sequence AAG AAC TCG TCA AGA AGG CGA TAG AAG GCG) and the
602 first exon of TOLLIP (Forward sequence: AGC TAC TGG GAG GCC ATA CA; Reverse sequence:
603 CGT GTA CGG GAG ACC CAT TT). Protein expression was confirmed in both knockout and
604 backcrossed alleles by qPCR and Western blot. All wild type control mice were age-matched
605 littermates to ensure a common genetic background.

606

607 *Model of Mtb aerosol infection*

608 Aerosol infections were performed with wildtype H37Rv Mtb or H37Rv Mtb with an mCherry
609 reporter plasmid. Mice were enclosed in a Glas-Col aerosol infection chamber and ~50-100 CFU
610 were deposited into mouse lungs. Doses were confirmed using control mice by plating lung
611 homogenates on 7H10 agar immediately after aersosol infection. Mice were sacrificed at
612 indicated timepoint, and lungs were gently homogenized in PBS-containing 0.05%Tween
613 using a gentleMacs dissociator (Miltenyi Biotec). Tissue homogenates were serially diluted on
614 7H10 agar and lung CFU was enumerated.

615

616 *Lung Cell Flow Cytometry*

617 Lung single cell suspensions were washed and stained for viability with Zombie Aqua viability
618 dye (BioLegend) for 10 min at room temperature in the dark. After incubation, 100 µl of a
619 surface antibody cocktail diluted in 50% FACS buffer/50% 24G2 Fc block buffer was added and
620 surface staining was performed for 30 min at 4°C. Antibody lists can be found in **Table S1**. The
621 cells were washed once with FACS buffer and fixed with 2% paraformaldehyde for 1 h prior to
622 analyzing on an LSRII flow cytometer (BD Biosciences). In some experiments, intracellular
623 staining was performed after surface staining. Permeabilization was peformed with Fix-Perm
624 buffer (eBiosciences) for minimum of 60 min before the addition of intracellular antibodies.
625 Then cells were fixed with 2% paraformaldehyde for 1 h prior to analyzing on an LSRII flow
626 cytometer (BD Biosciences). For cell sorting, mice were infected with Mtb H37Rv expressing
627 mCherry (gift of David Sherman). 28 days after infection, mice were sacrificed, and AM were
628 sorted on a BD FACSAria in a BSL-3 facility for infected and uninfected populations**.** The samples
629 were spun and stored -80° C in Trizol.

630

631 *Chimera Generation*

632 WT:*Tollip*$^{-/-}$ mixed bone marrow chimeras were generated in the following manner: WT B6.SJL-
633 Ptprca Pepcb/BoyJ (CD45.1+; Jax, Inc.) F1 mice were lethally irradiated (1000 cGy). A 1:1 mixture
634 of CD3-depleted (Miltenyi Biotec) *Tollip*$^{-/-}$ (CD45.2+) and F1 generation of C57BL/6J
635 (CD45.1+45.2+) bone marrow was provided intravenously. For full bone marrow chimera
636 generation, WT and *Tollip*$^{-/-}$ mice were irradiated, followed by hemopoietic reconstitution by
637 adoptive transfer of 5-10x10^{6} bone marrow cells via intravenous injection.

638

639 *Tissue Preparation and Evaluation*

640 Mice were euthanized and lungs were gently homogenized in HEPES buffer containing
641 Liberase Blendzyme 3 (70 µg/ml; Roche) and DNaseI (30 µg/ml; Sigma-Aldrich) using a
642 gentleMacs dissociator (Miltenyi Biotec). The lungs were then incubated for 30 min at 37°C and
643 then further homogenized a second time with the gentleMacs. The homogenates were filtered
644 through a 70 µm cell strainer, pelleted for RBC lysis with RBC lysing buffer (Thermo), and
645 resuspended in FACS buffer (PBS containing 2.5% FBS and 0.1% NaN_3). To prepare organs for
646 histology, lung sections were inflated to 15cm water pressure with 4% paraformaldehyde, fixed
647 in the same solution, embedded in paraffin and 4 m sections were generated. Sections stained
648 with hematoxylin and eosin were examined by a pathologist blinded to mouse genotype.

649

650 *Intracellular Mtb replication assay*.

651 Frozen Mtb was thawed and cultured on a shaking incubator for two doubling cycles. One day
652 prior to infection, cultures were back-diluted into an optical density (OD) of 0.2–0.4 in 7H9
653 media supplemented with glycerol (4%), Middlebrook ADC Growth Supplement (100 mL/L),
654 and Tween 80 (0.05%). At the time of infection, Mtb was filtered through a 5 µm syringe filter
655 to remove bacterial clumps, and cells were inoculated at indicated MOI. The inoculum was
656 prepared in RPMI-10 medium and applied to cells, which were centrifuged at 1200rpm for 5
657 minutes and incubated for 4 hours at 37°C. Supernatants were removed, and washed twice
658 with prewarmed PBS (phosphate-buffered saline) to remove unbound bacteria, before adding
659 per warmed RPMI supplemented with 10% FBS. Intracellular growth was determined using
660 luminescence on a Synergy H4 multimode microplate reader (Biotek Instruments) daily from

661 Day 0 to Day 3. In some experiments, 24hrs post infection cell culture supernatants were
662 collected and filtered twice using 0.22µm filter and frozen at -80°C.
663
664 *Macrophage Preparation*
665 Resident peritoneal cells, mainly consisting of *in vivo* differentiated macrophages, were isolated
666 using standard methods (Zhang, X et al 2008). Briefly, 10ml of cold PBS was injected using 27g
667 needle, and peritoneum was gently messaged. Cells were removed with PBS, centrifuged at 4°
668 C and placed into warm RPMI media. PEMs (1×10^5/well) were plated in 96-well plates in 200µL
669 of antibiotic-free RPMI 1640 containing with 10% Fetal Bovine Serum (Atlas Biologics). Cell were
670 rested for minimum 24hrs before further experimentation. Bone marrow was harvested from
671 mice and grown in RPMI supplemented with 10% heat inactivated FBS and M-CSF (40ng/ml) in
672 tissue culture treated plates. Cells were then incubated at 37° C for 6 to 7 days. Bone marrow-
673 derived macrophages (BMDM) were used after 7 days of culture. BMDMs were detached by
674 gently scrapping and cells were then plated in RPMI 1640 supplemented with 10% heat
675 inactivated FBS.
676
677 *Cellular Studies*
678 Cell-culture supernatants were collected at indicated time and frozen at -20℃ until analysis.
679 The cytokine concentrations in the culture supernatant were determined using quantitative
680 ELISA (Mouse TNF and IL-10 DuoSet; R&D Systems) as recommended by the manufacturer. For
681 detection of lipid bodies, PEMs from WT and *Tollip*$^{-/-}$ mice were plated (1×10^5/well) in a glass
682 bottom chamber slide. Lipid was added as previously described (*57*). Cells were washed twice
683 and resuspended in PBS solution of HCS LipidTOX Deep Red Neutral Lipid stain (ThermoFisher

684 Scientific) according to manufacturer instruction. After incubation, cells were washed twice
685 with PBS and fixed in 2% PFA for 30min. Cells were mounted in medium containing DAPI stain
686 (ProLong Gold, Thermo, Inc.). Lipid droplets were counted from 100 cells identified randomly
687 selected high-powered fields.
688
689 *Western blotting*
690 Immunoblots were performed as described previously (*58*). Briefly, 5-20µg of cell or tissue
691 protein extract was separated by SDS-PAGE, transferred onto PVDF membranes and
692 immunoblotted with primary antibodies, listed in **Table S1**. Secondary antibodies conjugated
693 to horseradish peroxidase were added and luminescence was quantitated.
694
695 *Preparation of total RNA and sequencing*
696 Total RNA from sorted cells was isolated using the manufacturer's instructions (TRIzol,
697 Invitrogen). The RNA purity and quantified was assessed by RNA-Tapestation (Agilent 4200).
698 cDNA was prepared using SMART-Seq v4 Ultra Low Input RNA Kit (Takara Bio USA, Inc). RNA
699 sequencing libraries were prepared using the Illumina TruSeq™ RNA Sample Preparation Kit
700 (Illumina, San Diego, CA, USA). Samples were sequenced as 50 bp paired-end reads on a
701 Illumina HiSeq 2500 and assessed using FastQC v0.11.8 to visualize sequence quality (*59*).
702 Sequences were filtered using AdapterRemoval v2.3.1 to remove adapters, remove sequences
703 with >1 ambiguous base, and trim ends to a 30+ Phred score (*60*). Sequences were aligned to
704 the mouse genome mm10 using STAR v2.7.4a (*61*), and alignments were assessed with Picard
705 v2.18.7 (*62*) and samtools v1.10 (*63*). Total reads in gene exons were quantified using
706 featureCounts v2.0.1 (*64*).

707

708 *Differential expression analysis*

709 Gene expression analyses were performed in R v3.6.1 with the tidyverse v1.3.0 (*65*). Overall,
710 samples were very high-quality with > 32 million aligned sequences per sample and low
711 variability in gene coverage (median coefficient of variation coverage < 0.6). Genes were
712 filtered to protein coding genes with biomaRt (N = 21850) with > 0.1 counts per million (CPM)
713 in at least three samples (N = 14215) (*66*). Counts were normalized for RNA composition using
714 edgeR and log2 CPM voom normalized with quality weights using limma (*67, 68*). Differentially
715 expressed genes were determined using limma using a contrasts model comparing WT and
716 *Tollip*$^{-/-}$ cells in uninfected and infected groups (**Table S2**). Genes with FDR < 0.3 for at least one
717 contrast (N = 3899) were clustered into modules using WCGNA (*69*) with a minimum R-squared
718 of 0.8 and minimum module size of 50. This resulted in 17 modules, leaving out 282 genes not
719 grouped into any module (**Table S3**). Module expression was calculated as the mean
720 expression of the log2 values of the genes within each module and assessed for differential
721 expression using the same contrasts model in limma. Modules were functionally assessed using
722 clusterProfiler v3.12.0 to compare them to the Broad Institute Hallmark gene sets in msigbr
723 v7.0.1 by hypergeometric distribution (*70, 71*). The Benjamini–Hochberg correction for multiple
724 comparisons was applied to P-values and significance was assessed at FDR < 0.05 for all tests.

725

726 *Statistics*

727 For mouse experiments, groups of five mice were compared with one another unless
728 otherwise indicated. Cellular measurements were compared using a two-sided
729 Students' *t* test unless otherwise specified. A value of $p < 0.05$ was considered a statistically

730 significant result unless otherwise specified. Statistics were calculated using Prism version 8.0

731 (GraphPad, Inc.).

732

733 **References and Notes**

734 1. K. Burns *et al.*, Tollip, a new component of the IL-1RI pathway, links IRAK to the IL-1
735 receptor. *Nat Cell Biol* **2**, 346-351 (2000).
736 2. K. Lu, I. Psakhye, S. Jentsch, Autophagic clearance of polyQ proteins mediated by
737 ubiquitin-Atg8 adaptors of the conserved CUET protein family. *Cell* **158**, 549-563
738 (2014).
739 3. M. L. Jongsma *et al.*, An ER-Associated Pathway Defines Endosomal Architecture for
740 Controlled Cargo Transport. *Cell* **166**, 152-166 (2016).
741 4. K. Chen, R. Yuan, Y. Zhang, S. Geng, L. Li, Tollip Deficiency Alters Atherosclerosis
742 and Steatosis by Disrupting Lipophagy. *J Am Heart Assoc* **6**, (2017).
743 5. A. C. Martini *et al.*, Amyloid-beta impairs TOM1-mediated IL-1R1 signaling. *Proc Natl*
744 *Acad Sci U S A* **116**, 21198-21206 (2019).
745 6. J. A. Shah *et al.*, Genetic Variation in Toll-Interacting Protein Is Associated With
746 Leprosy Susceptibility and Cutaneous Expression of Interleukin 1 Receptor Antagonist. *J*
747 *Infect Dis* **213**, 1189-1197 (2016).
748 7. J. A. Shah *et al.*, A Functional TOLLIP Variant is Associated with BCG-Specific
749 Immune Responses and Tuberculosis. *Am J Respir Crit Care Med*, (2017).
750 8. M. Ouimet *et al.*, Mycobacterium tuberculosis induces the miR-33 locus to reprogram
751 autophagy and host lipid metabolism. *Nat Immunol* **17**, 677-686 (2016).
752 9. M. G. Gutierrez *et al.*, Autophagy is a defense mechanism inhibiting BCG and
753 Mycobacterium tuberculosis survival in infected macrophages. *Cell* **119**, 753-766 (2004).
754 10. Y. Matsuzawa-Ishimoto, S. Hwang, K. Cadwell, Autophagy and Inflammation. *Annu Rev*
755 *Immunol* **36**, 73-101 (2018).

756 11. J. M. Kimmey *et al.*, Unique role for ATG5 in neutrophil-mediated immunopathology
757 during M. tuberculosis infection. *Nature* **528**, 565-569 (2015).
758 12. B. Levine, N. Mizushima, H. W. Virgin, Autophagy in immunity and inflammation.
759 *Nature* **469**, 323-335 (2011).
760 13. J. Grootjans, A. Kaser, R. J. Kaufman, R. S. Blumberg, The unfolded protein response in
761 immunity and inflammation. *Nat Rev Immunol* **16**, 469-484 (2016).
762 14. M. Costa-Mattioli, P. Walter, The integrated stress response: From mechanism to disease.
763 *Science* **368**, (2020).
764 15. S. E. Bettigole, L. H. Glimcher, Endoplasmic reticulum stress in immunity. *Annu Rev*
765 *Immunol* **33**, 107-138 (2015).
766 16. M. J. Kim *et al.*, Caseation of human tuberculosis granulomas correlates with elevated
767 host lipid metabolism. *EMBO Mol Med* **2**, 258-274 (2010).
768 17. B. Carow *et al.*, Spatial and temporal localization of immune transcripts defines
769 hallmarks and diversity in the tuberculosis granuloma. *Nat Commun* **10**, 1823 (2019).
770 18. C. Koumenis *et al.*, Regulation of protein synthesis by hypoxia via activation of the
771 endoplasmic reticulum kinase PERK and phosphorylation of the translation initiation
772 factor eIF2alpha. *Mol Cell Biol* **22**, 7405-7416 (2002).
773 19. N. Mizushima, M. Komatsu, Autophagy: renovation of cells and tissues. *Cell* **147**, 728-
774 741 (2011).
775 20. D. G. Russell, L. Huang, B. C. VanderVen, Immunometabolism at the interface between
776 macrophages and pathogens. *Nat Rev Immunol* **19**, 291-304 (2019).

777 21. F. J. Roca, L. J. Whitworth, S. Redmond, A. A. Jones, L. Ramakrishnan, TNF Induces
778 Pathogenic Programmed Macrophage Necrosis in Tuberculosis through a Mitochondrial-
779 Lysosomal-Endoplasmic Reticulum Circuit. *Cell* **178**, 1344-1361 e1311 (2019).
780 22. A. Kaser *et al.*, XBP1 links ER stress to intestinal inflammation and confers genetic risk
781 for human inflammatory bowel disease. *Cell* **134**, 743-756 (2008).
782 23. J. Oh *et al.*, Endoplasmic reticulum stress controls M2 macrophage differentiation and
783 foam cell formation. *J Biol Chem* **287**, 11629-11641 (2012).
784 24. A. J. Olive, C. M. Sassetti, Metabolic crosstalk between host and pathogen: sensing,
785 adapting and competing. *Nat Rev Microbiol* **14**, 221-234 (2016).
786 25. T. A. Seimon *et al.*, Induction of ER stress in macrophages of tuberculosis granulomas.
787 *PLoS One* **5**, e12772 (2010).
788 26. Y. J. Lim *et al.*, Mycobacterium tuberculosis 38-kDa antigen induces endoplasmic
789 reticulum stress-mediated apoptosis via toll-like receptor 2/4. *Apoptosis* **20**, 358-370
790 (2015).
791 27. S. Liang *et al.*, BAG2 ameliorates endoplasmic reticulum stress-induced cell apoptosis in
792 Mycobacterium tuberculosis-infected macrophages through selective autophagy.
793 *Autophagy* **16**, 1453-1467 (2020).
794 28. J. A. Shah *et al.*, Human TOLLIP Regulates TLR2 and TLR4 Signaling and Its
795 Polymorphisms Are Associated with Susceptibility to Tuberculosis. *Journal of*
796 *immunology* **189**, 1737-1746 (2012).
797 29. G. T. Consortium, Human genomics. The Genotype-Tissue Expression (GTEx) pilot
798 analysis: multitissue gene regulation in humans. *Science* **348**, 648-660 (2015).

799 30. J. A. Shah *et al.*, TOLLIP deficiency is associated with increased resistance to Legionella
800 pneumophila pneumonia. *Mucosal Immunol* **12**, 1382-1390 (2019).
801 31. M. Guilliams *et al.*, Alveolar macrophages develop from fetal monocytes that
802 differentiate into long-lived cells in the first week of life via GM-CSF. *J Exp Med* **210**,
803 1977-1992 (2013).
804 32. S. B. Cohen *et al.*, Alveolar Macrophages Provide an Early Mycobacterium tuberculosis
805 Niche and Initiate Dissemination. *Cell Host Microbe* **24**, 439-446 e434 (2018).
806 33. A. Liberzon *et al.*, The Molecular Signatures Database (MSigDB) hallmark gene set
807 collection. *Cell Syst* **1**, 417-425 (2015).
808 34. M. Ouimet *et al.*, Autophagy regulates cholesterol efflux from macrophage foam cells via
809 lysosomal acid lipase. *Cell Metab* **13**, 655-667 (2011).
810 35. D. Scheuner *et al.*, Translational control is required for the unfolded protein response and
811 in vivo glucose homeostasis. *Mol Cell* **7**, 1165-1176 (2001).
812 36. A. Krzyzosiak *et al.*, Target-Based Discovery of an Inhibitor of the Regulatory
813 Phosphatase PPP1R15B. *Cell* **174**, 1216-1228 e1219 (2018).
814 37. R. L. Hunter, On the pathogenesis of post primary tuberculosis: the role of bronchial
815 obstruction in the pathogenesis of cavities. *Tuberculosis (Edinb)* **91 Suppl 1**, S6-10
816 (2011).
817 38. R. L. Hunter, Tuberculosis as a three-act play: A new paradigm for the pathogenesis of
818 pulmonary tuberculosis. *Tuberculosis (Edinb)* **97**, 8-17 (2016).
819 39. D. G. Russell, P. J. Cardona, M. J. Kim, S. Allain, F. Altare, Foamy macrophages and the
820 progression of the human tuberculosis granuloma. *Nat Immunol* **10**, 943-948 (2009).

821 40. E. Balsa *et al.*, ER and Nutrient Stress Promote Assembly of Respiratory Chain
822 Supercomplexes through the PERK-eIF2alpha Axis. *Mol Cell* **74**, 877-890 e876 (2019).
823 41. J. Han *et al.*, ER-stress-induced transcriptional regulation increases protein synthesis
824 leading to cell death. *Nat Cell Biol* **15**, 481-490 (2013).
825 42. F. G. Almaguel *et al.*, Lipotoxicity-mediated cell dysfunction and death involve
826 lysosomal membrane permeabilization and cathepsin L activity. *Brain Res* **1318**, 133-143
827 (2010).
828 43. F. J. Roca, L. Ramakrishnan, TNF dually mediates resistance and susceptibility to
829 mycobacteria via mitochondrial reactive oxygen species. *Cell* **153**, 521-534 (2013).
830 44. S. Xu *et al.*, Palmitate induces ER calcium depletion and apoptosis in mouse podocytes
831 subsequent to mitochondrial oxidative stress. *Cell Death Dis* **6**, e1976 (2015).
832 45. K. F. Ferri, G. Kroemer, Organelle-specific initiation of cell death pathways. *Nat Cell*
833 *Biol* **3**, E255-263 (2001).
834 46. K. Kagedal, U. Johansson, K. Ollinger, The lysosomal protease cathepsin D mediates
835 apoptosis induced by oxidative stress. *FASEB J* **15**, 1592-1594 (2001).
836 47. E. Cantu *et al.*, Protein Quantitative Trait Loci Analysis Identifies Genetic Variation in
837 the Innate Immune Regulator TOLLIP in Post-Lung Transplant Primary Graft
838 Dysfunction Risk. *Am J Transplant* **16**, 833-840 (2016).
839 48. R. Ravindran *et al.*, Vaccine activation of the nutrient sensor GCN2 in dendritic cells
840 enhances antigen presentation. *Science* **343**, 313-317 (2014).
841 49. D. Schmid, M. Pypaert, C. Munz, Antigen-loading compartments for major
842 histocompatibility complex class II molecules continuously receive input from
843 autophagosomes. *Immunity* **26**, 79-92 (2007).

844 50. H. K. Lee *et al.*, In vivo requirement for Atg5 in antigen presentation by dendritic cells.
845 *Immunity* **32**, 227-239 (2010).
846 51. M. I. Whang *et al.*, The Ubiquitin Binding Protein TAX1BP1 Mediates Autophagasome
847 Induction and the Metabolic Transition of Activated T Cells. *Immunity* **46**, 405-420
848 (2017).
849 52. J. Wei *et al.*, Autophagy enforces functional integrity of regulatory T cells by coupling
850 environmental cues and metabolic homeostasis. *Nat Immunol* **17**, 277-285 (2016).
851 53. R. L. Hunter, Pathology of post primary tuberculosis of the lung: an illustrated critical
852 review. *Tuberculosis (Edinb)* **91**, 497-509 (2011).
853 54. V. Cornil, L. Ranvier, A manual of pathological histology translated with notes and
854 additions by EO Shakespeare and JHC Simms. *Philadephia: Henry C Lea*, 394-445
855 (1880).
856 55. J. G. Im, H. Itoh, K. S. Lee, M. C. Han, CT-pathology correlation of pulmonary
857 tuberculosis. *Crit Rev Diagn Imaging* **36**, 227-285 (1995).
858 56. A. Didierlaurent *et al.*, Tollip regulates proinflammatory responses to interleukin-1 and
859 lipopolysaccharide. *Mol Cell Biol* **26**, 735-742 (2006).
860 57. P. Peyron *et al.*, Foamy macrophages from tuberculous patients' granulomas constitute a
861 nutrient-rich reservoir for M. tuberculosis persistence. *PLoS Pathog* **4**, e1000204 (2008).
862 58. S. A. Soleimanpour *et al.*, The diabetes susceptibility gene Clec16a regulates mitophagy.
863 *Cell* **157**, 1577-1590 (2014).
864 59. S. Andrews. (2010).
865 60. M. Schubert, S. Lindgreen, L. Orlando, AdapterRemoval v2: rapid adapter trimming,
866 identification, and read merging. *BMC research notes* **9**, 88-88 (2016).

867 61. A. Dobin *et al.*, STAR: ultrafast universal RNA-seq aligner. *Bioinformatics (Oxford,*
868 *England)* **29**, 15-21 (2013).
869 62. . (Broad Institute, 2019).
870 63. H. Li *et al.*, The Sequence Alignment/Map format and SAMtools. *Bioinformatics*
871 *(Oxford, England)* **25**, 2078-2079 (2009).
872 64. Y. Liao, G. K. Smyth, W. Shi, featureCounts: an efficient general purpose program for
873 assigning sequence reads to genomic features. *Bioinformatics* **30**, 923-930 (2013).
874 65. H. Wickham *et al.*, Welcome to the Tidyverse. *Journal of Open Source Software* **4**, 1686-
875 1686 (2019).
876 66. S. Durinck *et al.*, BioMart and Bioconductor: a powerful link between biological
877 databases and microarray data analysis. *Bioinformatics* **21**, 3439-3440 (2005).
878 67. M. D. Robinson, D. J. McCarthy, G. K. Smyth, edgeR: a Bioconductor package for
879 differential expression analysis of digital gene expression data. *Bioinformatics (Oxford,*
880 *England)* **26**, 139-140 (2010).
881 68. M. E. Ritchie *et al.*, limma powers differential expression analyses for RNA-sequencing
882 and microarray studies. *Nucleic acids research* **43**, e47-e47 (2015).
883 69. P. Langfelder, S. Horvath, WGCNA: an R package for weighted correlation network
884 analysis. *BMC Bioinformatics* **9**, 559 (2008).
885 70. G. Yu, L.-G. Wang, Y. Han, Q.-Y. He, clusterProfiler: an R package for comparing
886 biological themes among gene clusters. *Omics : a journal of integrative biology* **16**, 284-
887 287 (2012).
888 71. I. Dolgalev. (2019).
889

890 **Abbreviations**

891 AM – alveolar macrophage

892 BafA – bafilomycin A

893 CFU – colony forming units

894 DC – dendritic cells

895 DEG – differentially-expressed genes

896 EIF2 – eukaryotic initiation factor 2

897 ER – endoplasmic reticulum

898 IM – interstitial macrophages

899 LD – lipid droplet

900 MA -- Mycolic acid

901 MDM – monocyte-derived macrophages

902 Mtb – *Mycobacterium tuberculosis*

903 PEM – peritoneal extract macrophages

904 PMN – neutrophils

905 TB – tuberculosis

906 TOLLIP – Toll-Interacting Protein

907 WT – wild-type

908 WGCNA – weighted gene coexpression network analysis

909

910 **Acknowledgements:**

911 The authors wish to thank the University of Washington Center for Lung Biology Histology and

912 Imaging Core for their helpful advice on pathology staining and analysis. We are grateful to the

913 Seattle Children's Research Institute Cell Sorting Core for their assistance and technical support.
914 **Funding:** This work was supported by the NIH (R01 AI136912 to JAS; R01 DK108921 to SAS)
915 and the Department of Veterans Affairs (I01 BX004444 to SAS). GLP was supported by the
916 American Diabetes Association (19-PDF-063). **Author Contributions:** Conceptualization: SV,
917 KU, SS JS; methodology: SV, SS, KU, MA, SD, JS; resources: JS, software: KDM, MA; validation: SV,
918 JS, RE; formal analysis: MA, KDM; investigation: SV, SH, CP, GP, AL, AP, RP, JS; writing – original
919 draft: SV, JS; writing – review and editing: KU, SS, MA, CP, JS; supervision: JS, KU, MA, SS; project
920 administration: SV, JS; funding acquisition: JS, KU, SS, MA. Competing Interests: The authors
921 declare no competing interests. Data and materials availability: All data from this study are
922 available by request to jashah@uw.edu. Abbreviations and description of bioinformatics tools
923 and all bioinformatic data and code can be found at https://github.com/altman-lab/JS20.01.
924

925 **Figure 1: TOLLIP is required for Mtb control in mice and its absence induces foam cell**
926 **formation.** Mice were infected with Mtb H37Rv (50-100 cfu) via aerosol and monitored over
927 time. **A)** Experimental timeline. **B-C)** Lung bacterial burden in WT (*clear circle*) and *Tollip*$^{-/-}$ (*black*
928 *square*) mice **B)** 1-2 weeks and **C**) 4 weeks and later after infection. Spleen bacterial burden **D**)
929 1-2 weeks and **E)** 4 weeks and later after infection. * $p < 0.05$; ** $p < 0.01$, ***$p < 0.001$, two-
930 sided t-test at each time point; n = 5 mice/group. Overall associations were determined using
931 a two-sided ANOVA accounting for time and genotype. **F)** Survival curve analysis of WT (*clear*
932 *circle*) and *Tollip*$^{-/-}$ (*black square*) mice after aerosol infection with 50-100cfu Mtb H37Rv strain.
933 N = 10 mice/group. $P < 0.0001$, Mantel-Cox test. **G)** Percentage of initial body weight after Mtb
934 aerosol infection *Circle* – WT mice; *square* - *Tollip*$^{-/-}$ mice. N = 10 / group. **H)** Hematoxylin and
935 eosin staining of Mtb-infected lung tissue from WT and *Tollip*$^{-/-}$ mice 4 and 8 weeks after aerosol

936 infection. **I)** Experimental outline of full bone marrow chimera experiments. **J)** Lung bacterial
937 burden of bone marrow chimeric mice, 8 weeks after aerosol Mtb infection. N = 5 mice/group.
938 * $p < 0.05$, ** $p < 0.01$, *** $p < 0.001$.
939
940 **Figure 2: Mtb preferentially infects *Tollip*$^{-/-}$ myeloid cells 8 weeks after aerosol infection.**
941 Lungs from Mtb-infected mice were gently dissociated, and flow cytometry was performed.
942 Gating strategy described in **Figure S2**. The proportion of lung resident myeloid cells from WT
943 (*clear circle*) and *Tollip*$^{-/-}$ (*black square*) mice was compared **A)** 4 and **B)** 8 weeks after aerosol
944 infection with 50-100 cfu mCherry-expressing Mtb. The proportion of each cell subset infected
945 with Mtb (mCherry+) was compared between groups **C)** 4 and **D)** 8 weeks post infection. N = 5
946 mice/group. Experiment was performed three times independently. Statistical significance
947 determined using Student's t-test. AM – alveolar macrophage, MDM – monocyte-derived
948 macrophage, IM – interstitial macrophage, PMN – neutrophil, DC – dendritic cell.
949
950 **Figure 3: *Tollip*$^{-/-}$ lung-resident myeloid cells develop enhanced antimicrobial responses**
951 **after Mtb infection.** Please see **Supplemental Figure 2** for gating strategy to identify myeloid
952 cell subsets. **A and B)** Intracellular NOS2 protein expression was measured in Mtb-infected
953 lung-resident myeloid cells (mCherry+) by flow cytometry **A)** 4 and **B)** 8 weeks post infection.
954 CD80 expression was measured **C)** 4 and **D)** 8 weeks post infection. Median fluorescence
955 intensity was compared using a two-sided t-test. N = 5 mice/group. WT (*clear circle*); *Tollip*$^{-/-}$
956 (*black square*). Experiment was repeated three times independently. AM – alveolar
957 macrophage, MDM – monocyte-derived macrophage, IM – interstitial macrophage, PMN –
958 neutrophil, DC – dendritic cell.

959

960 **Figure 4. *Tollip*$^{-/-}$ AM become preferentially infected with Mtb over time.** WT:*Tollip*$^{-/-}$ mixed
961 bone marrow chimeric mice were infected with Mtb expressing mCherry (50-100 cfu) and
962 followed. Gating strategy can be found in **Figure S3**. **A)** Experimental strategy and timeline.
963 Mixed bone marrow chimeras were generated by mixing 1:1 ratios of WT (CD45.1+/CD45.2+)
964 and *Tollip*$^{-/-}$ (CD45.2+) mice and transferred to a CD45.1+ murine host. **B)** Frequency distribution
965 of CD45 expression in naïve mixed bone marrow chimeric mice. **C)** Composition of mCherry+
966 lung leukocytes at the indicated time point. **D and E)** Distribution of mCherry+ cells at **D)** d14
967 and **E)** d28 post-infection in mixed bone marrow chimeric mice. **F)** Median fluorescence
968 intensity of nitric oxide synthase (NOS) in AM at d28 post-infection from mixed bone marrow
969 chimeric mice. N = 4 or 5 mice for each time point as indicated; experiments were conducted
970 three times independently. * $p < 0.05$, ** $p < 0.005$. Significance determined by paired two-
971 sided t-test. AM – alveolar macrophage, MDM – monocyte-derived macrophage, IM –
972 interstitial macrophage, PMN – neutrophil.

973

974 **Figure 5. Global gene expression analysis of Mtb-infected *Tollip*$^{-/-}$ AM 28 days after**
975 **infection demonstrates increased EIF2 signaling.** Mixed bone marrow chimeric mice were
976 infected with mCherry-expressing Mtb and 28 days after infection, Mtb-infected and Mtb-
977 uninfected WT and *Tollip*$^{-/-}$ AM were sorted and RNA-seq was performed. Sorting strategy can
978 be found in **Figure S3**. **A)** Volcano plot of gene expression (log2 fold change) and significance
979 (-log10(FDR)) for genes between *Tollip*$^{-/-}$ (CD45.2) and WT (CD45.1+CD45.2+), Mtb-uninfected
980 and **B)** Mtb-infected AMs. Horizontal lines indicate significant genes (FDR < 0.05) and genes
981 used in WGCNA modules (FDR < 0.3) **C)** Heatmap of mean module z-score for infection:

982 TOLLIP groups. Red bars indicate increased expression in *Tollip*$^{-/-}$ AM and blue bars indicated
983 decreased expression in *Tollip*$^{-/-}$ AM, separated by infection status. Modules (columns) were
984 average hierarchical clustered. **D)** Heat map of enrichment of significant Hallmark gene sets
985 (FDR q-value < 0.05) in modules. Color indicates percent of genes in a module that mapped to
986 a given Hallmark. The total number of genes in each module is indicated above. Modules
987 (columns) were clustered as in **C)** and Hallmark terms (rows) were average hierarchical
988 clustered based on enrichment percentages. Red and blue bars are as in **C)**. **E-F)** Bar graph of
989 the Hallmark terms enriched in modules with **E)** increased expression in Mtb-infected, *Tollip*$^{-/-}$
990 AM or **F)** decreased expression in both Mtb-infected and bystander AM. Bar length indicates
991 the proportional enrichment of each pathway. Color indicates degree of significance: *purple* –
992 FDR q < 10^{-16}; *red* -- q < 10^{-8}; *orange* – q < 10^{-4}. **G)** Ingenuity Pathway Analysis of upstream
993 regulatory pathways enriched by data for Mtb-infected cells. *Orange* bar indicates increased
994 expression in *Tollip*$^{-/-}$ AM. *Gray* bars indicate no directional data available.
995
996 **Figure 6. *Tollip*$^{-/-}$ AM accumulate excess lipid that creates a permissive environment for**
997 **Mtb replication.** Bone marrow from WT (*black bars*) or *Tollip*$^{-/-}$ (*white bars*) were differentiated
998 *ex vivo* to macrophages using 40ng/mL mCSF for 7-9 days. Following differentiation, BMDMs
999 were treated for 6hr with or without 250nM Bafilomycin A (BafA). **A**) Representative western
1000 blot results showing protein levels of LC3I/II and p62. **B**) Quantification of protein levels (by
1001 densitometry) of LC3II using total LC3 (I+II) as a loading control. ***p<0.001 2-way ANOVA for
1002 an effect of BafA **C**) Quantification of p62 levels (by densitometry) using vinculin as a loading
1003 control. p=0.056 2-way ANOVA effect of BafA. **D-F**) WT and *Tollip*$^{-/-}$ peritoneal exudate
1004 macrophages (PEM) were isolated and incubated with mixed mycolic acids (MA) for 72hrs.

1005 PEM were stained with LipidTOX Red dye (*red*) and DAPI (*blue*), fixed, and visualized with
1006 fluorescent microscopy. **D)** Representative image for of lipid droplet (LD) accumulation in WT
1007 and *Tollip*$^{-/-}$ PEM. **E)** Percentage of cells with visible LD, of 100 cells imaged. Bar – error bars
1008 (mean ± SD). **F)** Total number of LD per cell, of 100 cells with detectable LD. Bar – error bars
1009 (mean ± SD). **G)** Median fluorescence intensity of alveolar macrophages (AM) and monocyte-
1010 derived macrophages (MDM) stained with LipidTox neutral lipid stain from mixed bone
1011 marrow chimeric mice 28 days after Mtb infection. Infection and gating were performed as in
1012 **Figure 5**. Lines connect WT and *Tollip*$^{-/-}$ AM from the same mouse. Significance calculated
1013 using two-sided paired t-test. **H)** Representative histogram of AM and MDM lipid staining
1014 from one experiment (WT – blue; *Tollip*$^{-/-}$ – red). **I** Luminescence over time in WT and *Tollip*$^{-/-}$
1015 PEM's incubated with exogenous lipid - MA, mycolic acid (10µg/ml) and infected with Mtb
1016 H37Rv expressing *lux* luminescence gene (MOI 1). PEMs were isolated and incubated with MA
1017 for 72 hr before infection. Intracellular replication was measured by luminescence for each
1018 group over the next three days in quadruplicate and repeated three times to assess
1019 reproducibility. Statistical significance was determined by 3-way ANOVA accounting for time,
1020 genotype, and lipid administration.
1021
1022 **Figure 7. EIF2 activation impairs Mtb control in macrophages.** Peritoneal extract
1023 macrophages (PEM) were plated and infected with Mtb expressing the lux luminescence
1024 plasmid (MOI 1). For each experiment luminescence was measured at the time points
1025 described. A) WT PEM were treated with vehicle control or raphin-1 (10µM) at the time of
1026 infection. Luminescence was measured over time. Statistical significance determined by 2-
1027 way ANOVA accounting for time and treatment. B) WT PEM were treated with mycolic acid

1028 (MA; 10µg/ml) for 72hr, then treated with either vector control or raphin-1 at the time of Mtb
1029 infection. Bars represent luminescence at 72hr after infection. Statistical significance
1030 determined by 2-way t-test. C) WT and *Tollip*$^{-/-}$ PEM were treated with vehicle control or
1031 raphin-1, infected with Mtb, then luminescence was measured over time. Statistical
1032 significance determined by 3-way ANOVA accounting for TOLLIP expression, time, and
1033 treatment. D) *Tollip*$^{-/-}$ PEM were treated with MA, raphin-1, or vehicle control as in B).
1034 Luminescence was measured 72h after infection. Statistical significance determined by two-
1035 sided unpaired t-test. Experiments were performed six times, all data is shown. * $p < 0.05$, ** p
1036 < 0.01.
1037
1038 **Figure 8. EIF2 kinases are enriched in caseous TB granulomas.** Expression of A) *EIF2AK1*, B)
1039 *EIF2AK2*, C) *EIF2AK3*, D) *EIF2AK4*, E) *EIF2S1, and* F) *TOLLIP* in human caseous granuloma tissue,
1040 compared with healthy appearing lung tissue from different lobes from the same individuals.
1041 N = 7. Data are derived from the analysis of the publicly available GEO dataset GSE20050
1042 using the indicated probe sets. FDR – false discovery rate. FDR is indicated above each data
1043 point.
1044
1045 **Supplemental Materials:**
1046
1047 **Figure S1.** TOLLIP deficiency induces a proinflammatory cytokine bias in Mtb-infected
1048 macrophages. Peritoneal exudate macrophages (PEM) were isolated, plated in tissue culture,
1049 and stimulated with LPS (10 ng/ml), PAM3 (250 ng/ml), and Mtb whole cell lysate (1mcg/ml)
1050 overnight. Cell culture supernatants (mean ± SD) were obtained and **A)** TNF and **B)** IL-10

1051 concentrations were measured by ELISA. PEM were infected with Mtb H37Rv (MOI 2.5)
1052 overnight, then cell culture supernatants were collected and **C)** TNF, **D)** IL-1β and **E)** IL-10 were
1053 measured by ELISA (mean ± SD). Two-sided t-test was used to determine statistical significance
1054 between groups. N=3/group, experiment was performed three times independently.
1055
1056 **Figure S2.** Lists flow cytometry gating strategy for Figure 3.
1057
1058 **Figure S3.** Lists flow cytometry gating strategy for Figure 5.
1059
1060 **Figure S4.** Describes sorting strategy for Figure 6.
1061
1062 **Figure S5.** Describes colocalization of Mtb and LC3 with Mtb in control and TOLLIP-deficient
1063 THP-1 cells.
1064
1065 **Figure S6.** Demonstrates increase in cellular stress in lipid-enriched, Mtb infected, Tollip-/-
1066 macrophages.
1067
1068 **Table S1.** Key Resources Table.
1069
1070 **Data File S1.** List of differentially expressed genes (DEG) in Mtb- infected and Mtb-uninfected
1071 *Tollip*$^{-/-}$ AM compared to WT AM from the same mice.
1072

1073 **Data File S2.** List of genes in each WGCNA module comparing sorted WT and *Tollip*$^{-/-}$ AM.

1074

1075 **Data File S3.** List of GSEA hallmark pathways significantly enriched in each WGCNA module

1076 comparing sorted WT and *Tollip*$^{-/-}$ AM.

1077